



# Whole-rock chemistry and Sr isotope concentrations in the Upper Cretaceous shale, western Iran: evidence for a transition from trench to fore-arc setting

Hadi Amin-Rasouli<sup>1</sup> · Hossein Azizi<sup>2</sup> · Yoshihiro Asahara<sup>3</sup> · John S. Armstrong-Altrin<sup>4</sup> · Shahla Mahmodyan<sup>1</sup>

Received: 12 March 2022 / Accepted: 12 August 2022 / Published online: 12 September 2022  
© Saudi Society for Geosciences 2022

## Abstract

Upper Cretaceous Sanandaj (UCS) units (K8–K12) in the northern Sanandaj-Sirjan Zone, west Iran, which consists of ~2,000 meters of shale, sandstone, limestone, conglomerate, and pyroclastic rocks, with interbedded basalticandesitic lava. The Rb–Sr whole-rocks isochron for nine shale samples shows an age of  $125 \pm 39$  Ma with an initial  $^{87}\text{Sr}/^{86}\text{Sr} = 0.7106 \pm 0.0032$ . The chemical compositions of the shale samples show average values of 71.8 wt.%  $\text{SiO}_2$ , 17.1 wt.%  $\text{Al}_2\text{O}_3$ , 4.8 wt.%  $\text{Fe}_2\text{O}_3$ , 0.3 wt.% CaO, and 1.7 wt.%  $\text{Na}_2\text{O}$ . The  $\text{SiO}_2\text{--Al}_2\text{O}_3 + \text{Na}_2\text{O} + \text{K}_2\text{O}$  and Th/Sc–Zr/Sc diagrams for samples reflect low sediment maturity, and the shale components were deposited by the first sedimentary cycle. The REEs Chondrite-normalized patterns reveal higher LREEs contain ( $\text{La}/\text{Yb}_{\text{CN}} = 10.5$ ), flat HREEs, negative Eu anomaly ( $\text{Eu}/\text{Eu}^*_{\text{SN}} = 0.26\text{--}0.89$ ), and Nb anomaly ( $\text{Nb}/\text{Nb}^*_{\text{SN}} = 0.14\text{--}0.82$ ). Also, the ratios of  $\text{Al}_2\text{O}_3/\text{TiO}_2$  (18–22),  $\text{La}/\text{Lu}_{\text{CN}}$  (5.43–24.4),  $\text{La}/\text{Sc}$  (0.51–2.53), Th/Sc (0.42–0.68), and LREEs/HREEs ( $\text{Nd}/\text{Er}_{\text{CN}} > 5$ ), suggesting these rocks were dominantly derived from intermediate-acidic rocks in an active continental margin. Meanwhile, Ni/Co (5.6–9.9),  $\text{V}/(\text{V} + \text{Ni})$  (0.64–0.90), and  $\text{Mn}^*$  (–3.6 to –6.6) values reveal that shale layers were deposited in a sediment-starved basin under reducing conditions during the Late Cretaceous contemporaneous with volcanic activities. Upwelling of the anoxic water due to volcanic events has led to an oceanic anoxic event, the demise of micro-organisms, and the deposition of organic-rich black shale. The UCS shale geochemistry and the vertical stacking pattern of the K8–K12 units show that their tectonic settings have been changed from a trench to a fore-arc from bottom to top. These transitions are related to the continent-ward migration of the magmatic arc.

**Keywords** Sanandaj shale · Sanandaj-Sirjan zone · Geochemistry · Trench basin · Fore-arc basin · Sr isotope ratios

## Introduction

Black shales are fine-grained clastic sedimentary rocks enriched in organic matter (e.g., Trabucho-Alexandre et al. 2012). They can form in various tectonic and depositional settings, especially in anoxic deep-water environments (e.g., Martinez 2003; Jenkyns 2010). The UCS shale is widely spread northwest of the Sanandaj-Sirjan Zone (SaSZ). Great igneous provinces were established in this area during the Cretaceous, suggesting that volcanic activity was responsible for black shale deposits (e.g., Ohkouchi et al. 2015). During this time, the NW-ward subduction of the Neo-Tethyan crust beneath Central Iran formed a subsiding extensional basin in the Northern SaSZ (N-SaSZ) (Azizi and Moinevaziri 2009).

The UCS succession (K8–K12 units) includes about 2000 m of black shale (mainly), sandstone, conglomerate, limestone, pyroclastic, and basaltic–andesitic lava. To date, geochemical investigations have not been performed on the

Responsible Editor: Attila Ciner

✉ Hadi Amin-Rasouli  
h.aminrasouli@uok.ac.ir

- <sup>1</sup> Department of Earth Sciences, Faculty of Sciences, University of Kurdistan, Sanandaj, Iran
- <sup>2</sup> Department of Mining Engineering, Faculty of Engineering, University of Kurdistan, Sanandaj, Iran
- <sup>3</sup> Department of Earth and Environmental Sciences, Graduate School of Environmental Studies, Nagoya University, Nagoya, Japan
- <sup>4</sup> Institute of Marine and Limnological Sciences, Universidad Nacional Autónoma de México, Ciudad de México, Mexico

Sanandaj shale. In this study, the whole-rock chemistry and Sr isotope ratios of the shale rocks, part of the UCS units, and the stacking pattern of their units have been investigated. Shale rocks record the geological evolution of the region (e.g., McLennan et al. 1993) and provide valuable information for understanding the paleoclimate, source-area weathering, paleoredox conditions, source rocks, tectonic settings, and geodynamic evolution of the basin (McLennan 1989). So, this investigation is significant for paleogeographic reconstructions of the Sanandaj-Sirjan Zone.

### Geological setting

The Sanandaj-Sirjan Zone (SaSZ), the most active zone in the Iranian plate (Stöcklin and Nabavi 1972), extends about 1500 km from the northwest (Sanandaj) to the southeast (Sirjan) with a width of 150–250 km (Stöcklin and Nabavi 1972; Mehdipour Ghazi and Moazzen 2015). It comprises

the critical events in the formation and evolution of the Neotethys basin (Hassanzadeh and Wernicke 2016). This basin opened in the Late Paleozoic and closed from the Late Cretaceous to the mid-Tertiary, due to convergence and continental collision between the Arabian and Iranian plates (e.g., Shahabpour 2005; Agard et al. 2005, 2011).

The SaSZ was an active Andean-type margin (Berberian and King 1981; Şengör 1990; Ao et al. 2016). More than 2000 m of Upper Cretaceous deposits, known as Sanandaj shale, are distributed in the north SaSZ. The Sanandaj shale facies show shallowing upward from distal turbidites to shallow marine carbonate facies. This unit is flanked on one side by the Urumieh–Dokhtar magmatic arc, UDMA, and on the other side by the deformed strata, including mélangé and blueschists, of a coeval subduction complex (Fig. 1A).

Alavi (1994; 2004; 2007) suggested that the northeastern boundary of the SaSZ with UDMA is the suture zone between the Afro-Arabian and Iranian plates. Based on his opinion, the SaSZ represents a thrust fault zone that has transported various rocks during the collision events. These

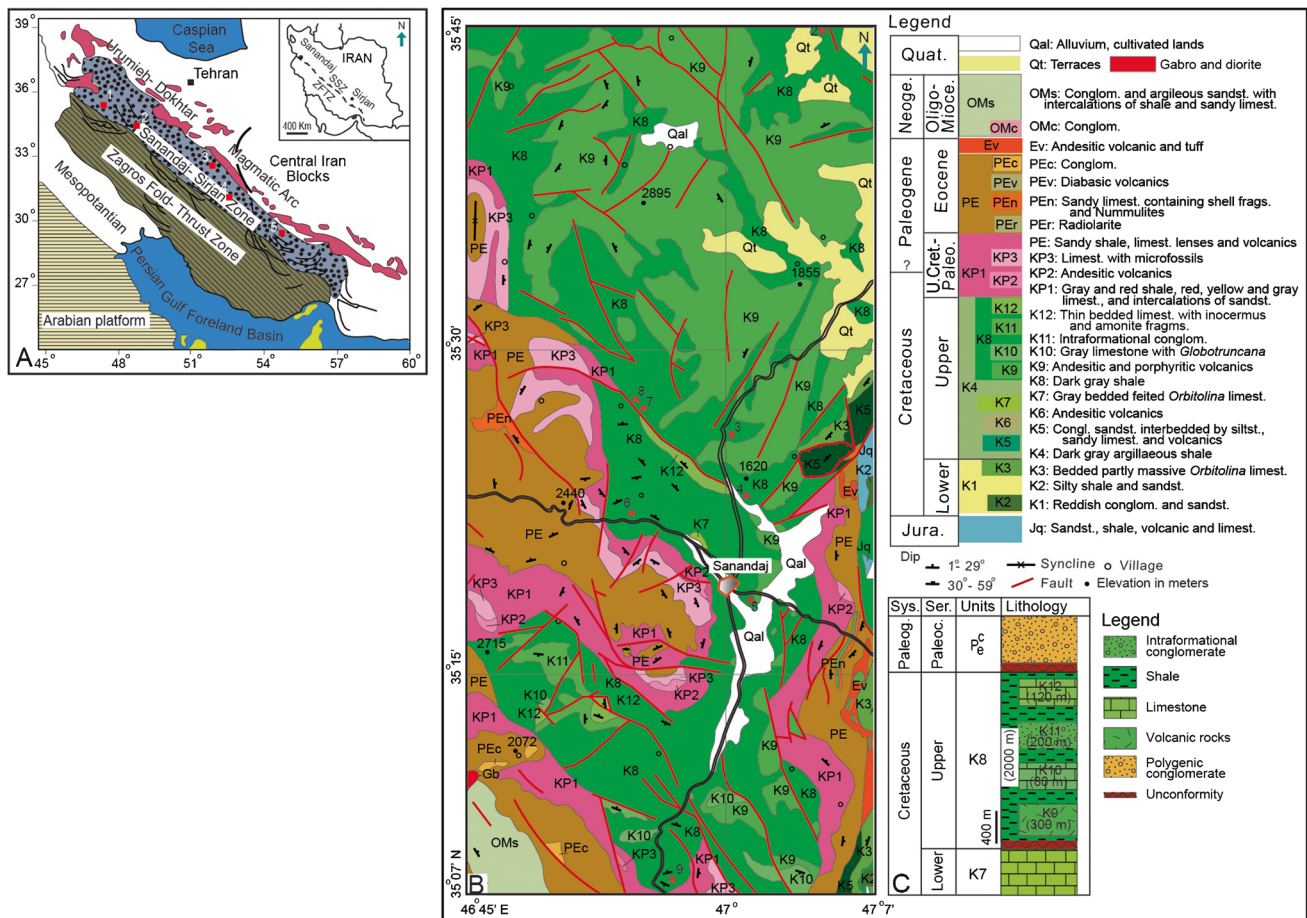


**Fig. 1** (A) Main geotectonic units in the Iranian plate (after Alavi 1994) and the location of Sanandaj (1), Hamadan (2), Esfahan (3), Abadeh (4), and Sirjan (5) areas. (B) Geological map of the study

area, showing the location of sampling points. (C) Stratigraphic column of UCS near the Sanandaj city (after Zahedi and Hajian 1985)

rocks include Cretaceous-Tertiary terrigenous, carbonate, and volcaniclastic strata. Several researchers (e.g., Berberian and King 1981; Şengör 1990; Mohajjel and Ferguson 2000; Hessami et al. 2001; Talebian and Jackson 2004) considered the boundary between the SaSZ and the Zagros Fold-Thrust Zone as the suture zone between these plates. Cherven (1986) proposed that Sanandaj shale is a pre-collision Cretaceous fore-arc deposit.

## Stratigraphy

The N-SaSZ mainly includes Upper Jurassic-Cretaceous rocks in Kurdistan province (Fig. 1B, C). Paleozoic rock outcrops are rare in the northwestern part of the SaSZ, whereas they are common in the southeastern segment of this zone (e.g., Azizi and Stern 2019). The Jurassic SaSZ rocks include phyllite and volcanic rocks with a low-to-moderate metamorphic imprint, except close to large-scale Mesozoic granitoid bodies (Azizi and Jahangiri 2008; Dargahi et al. 2010; Azizi and Asahara 2013; Azizi and Stern 2019). The mafic to felsic igneous Jurassic rocks are widespread and exposed, from the northwest to the southeast, in the Sanandaj, Hamadan, Esfahan, Abadeh, and Sirjan areas. Several geologists believed that these rocks are related to the northward Neotethys oceanic crust subduction beneath the Central Iranian plateau (Hassanzadeh and Wernicke 2016; Azizi et al. 2019).

Barremian-Aptian limestones, including orbitolina (K7), unconformably overlies the Jurassic complex and underlies, with the same contact by the UCS units in N-SaSZ (Stöcklin 1968). The UCS has undergone a low-grade metamorphic phase and consists of 5 units (Zahedi and Hajian 1985). The units include (a) K8; known as the Sanandaj shale; dark gray, yellow shale, silty shale with minor sandstone, and biomicrite, including Cenomanian pelagic microfossils, (b) K9; volcanic rocks with interbedded basaltic-andesitic lava and pyroclastic rocks, (c) K10; thin-bedded pelagic limestone with *Globotruncana*, (d) K11; graded bedding conglomerate, sandstone, siltstone, and (e) K12; thin-bedded limestone with inoceramus and ammonite fragments. The UCS is unconformably overlain by widespread, polygenic, nonmarine conglomerates of Paleocene age, (PEc; Figs. 1C and 2A-I).

## Petrography

### Description and interpretation

The UCS units in the study area comprise volcanic and sedimentary rocks. The volcanic rocks are green andesite and andesitic basalt with a porphyritic texture. The phenocryst

minerals are plagioclase (main mineral), k-feldspar, clinopyroxene, hornblende, and biotite. They are mainly altered to epidote, calcite, and sericite (Fig. 3A–C). The volcanic rocks have the typical characteristics of an island arc (Azizi and Asahara 2013).

The sedimentary rocks of the UCS consist of carbonate (pelagic and calciturbidite) and siliciclastic facies. The siliciclastic facies contain black shale, graywacke, and intraformational conglomerate. The shale facies is dark-colored laminated mudstone (Fig. 2A–D), containing Upper Cretaceous planktonic foraminifera, organic matter, silt-size quartz, biotite, clay, pyrite, and calcite (Fig. 3D, E). This facies also has several types of Nerites ichnofossils (Uchman et al. 2005), including *Paleodictyon isp.*, *Helminthorhapha isp.*, *Spirorhapha isp.*, and *Cosmorhapha isp.* (Fig. 2E, F). These characterizations and the absence of benthic fossils in their components reflect that shale facies was deposited in a deep marine under reducing conditions (Rodríguez-Tovar et al. 2010).

Graywacke facies has an erosional base with intraformational pebbles and fines upward to shale facies. The facies include poorly sorted angular to subangular volcanic and quartz grains in a fine-grained matrix which was deposited in the fore-arc basin by turbidity currents (Fig. 3F, G).

The intraformational conglomerates are lens-shaped bodies in the shale unit and contain abundant shale clasts derived from the syn-sedimentary intrabasinal tectonic high (Fig. 2J). These conglomerates are interpreted as gravitational deposits emplaced on a dipping submarine slope. Ghasemi and Talbot (2006) proposed that these conglomerates are associated with the increased Neotethys subduction rates beneath the SaSZ.

The pelagic carbonate facies include gray thin-bedded, bioturbated planktonic foraminifera-packstone to mudstone. These characteristics and the abundance of pyrite in the samples indicate that accumulation occurred under reducing conditions (Fig. 3H). The calciturbidite facies are thin-to-medium-bedded, interbedded with shale, representing the sharp basal contact, and become fining upward grain-supported to mud-supported textures. They contain planktonic foraminifera and benthic open-marine bioclasts, including echinoid and rudist fragments. The benthic bioclasts originated from the platform margin and were deposited as debris in the basin (Fig. 3I).

## Analytical technique

After studying thin sections, nine shale samples were collected from the K8 unit for chemical and isotopic analyses (Table 1 and 2). The samples were powdered and then washed with H<sub>2</sub>O<sub>2</sub> and 0.5 N HCl to remove organic matter and limestone components, respectively. The remaining fractions were used for the geochemical analysis.

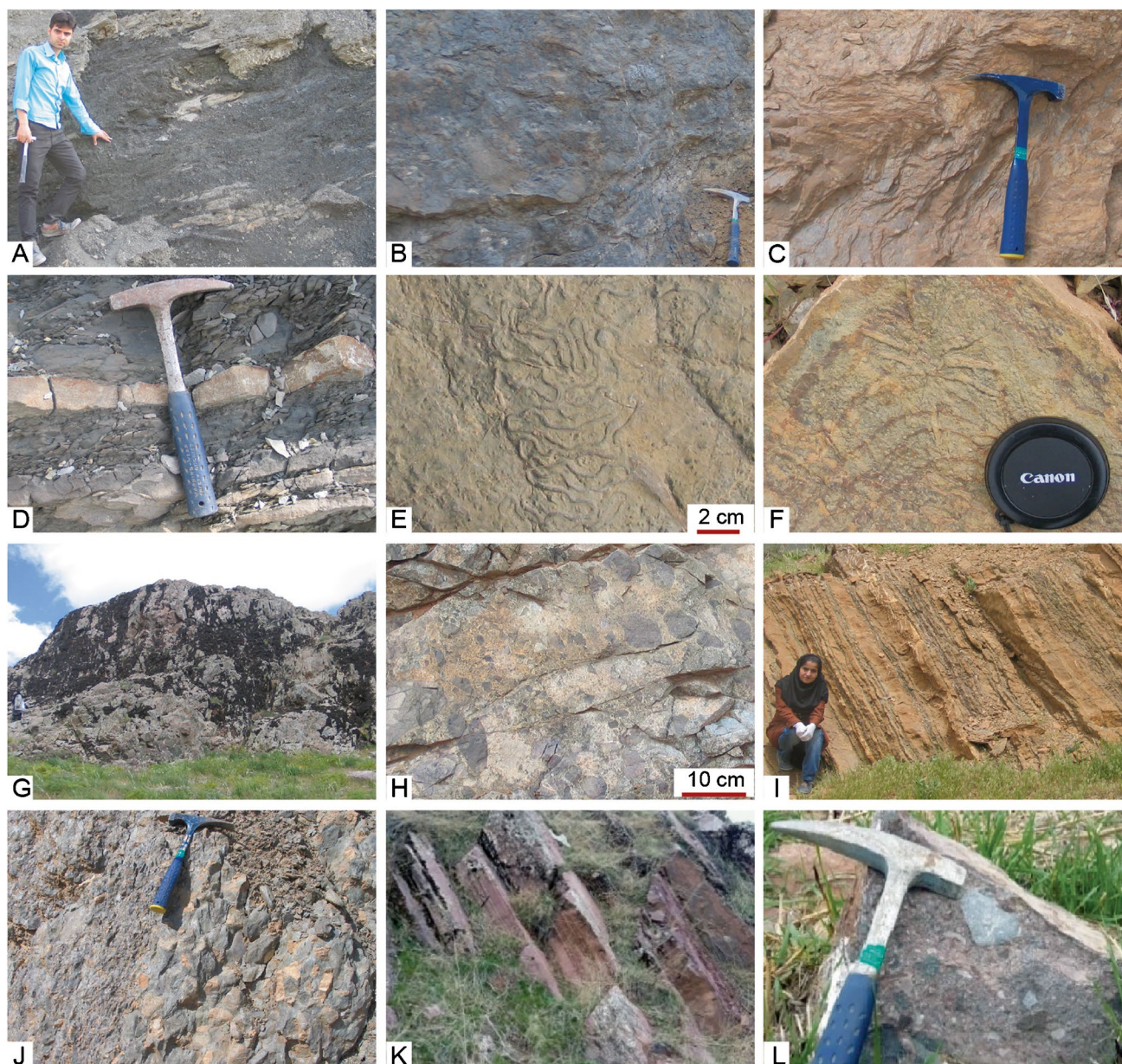


**Fig. 2** (A–D) Photographs of the Sanandaj shale unit, K8 (view to the southwest). (E, F) Field photographs of *Nerites* ichnofacies. (G) Photograph showing the andesitic volcanic rocks, K9 (view to the northeast). (H) Close-up view of the volcanic breccia, K9. (I) Field photograph of the K10 composed of pelagic limestone interlayered with shale. (J)

Close-up view of intraformational conglomerate, K11. (K) Photograph of thick-bedded to massive polygenic, nonmarine conglomerate. (L) Close-up view of the Paleocene polygenic conglomerate

Geochemical analyses were carried out at Nagoya University, Japan. For major element analysis, a mixture of 0.50 g of sample powder and 5.0 g of lithium tetraborate was prepared and melted at 1200 °C for 12–17 min using a high-frequency bead sampler (Rigaku) to make a glass bead. Major element compositions for the samples were measured using a WD-XRF spectrometer, Rigaku ZSX Primus II, on the fused beads (Table 3).

For analyses of trace element compositions and Sr isotope ratios, approximately 100 mg of each pulverized sample was decomposed with 3 ml of HF (38%) and 0.5–1 ml of HClO<sub>4</sub> (70%) in a covered polytetrafluoroethylene (PTFE) beaker at 120–140 °C. Then, the dissolved samples were dried at 140–160 °C on the hot plate with infrared lamps. After that, the samples were dissolved in 10 ml of 2–6 M HCl. The resulting solutions were split into two portions: one for the quantitative analysis of trace elements and the other for Sr isotope analysis.

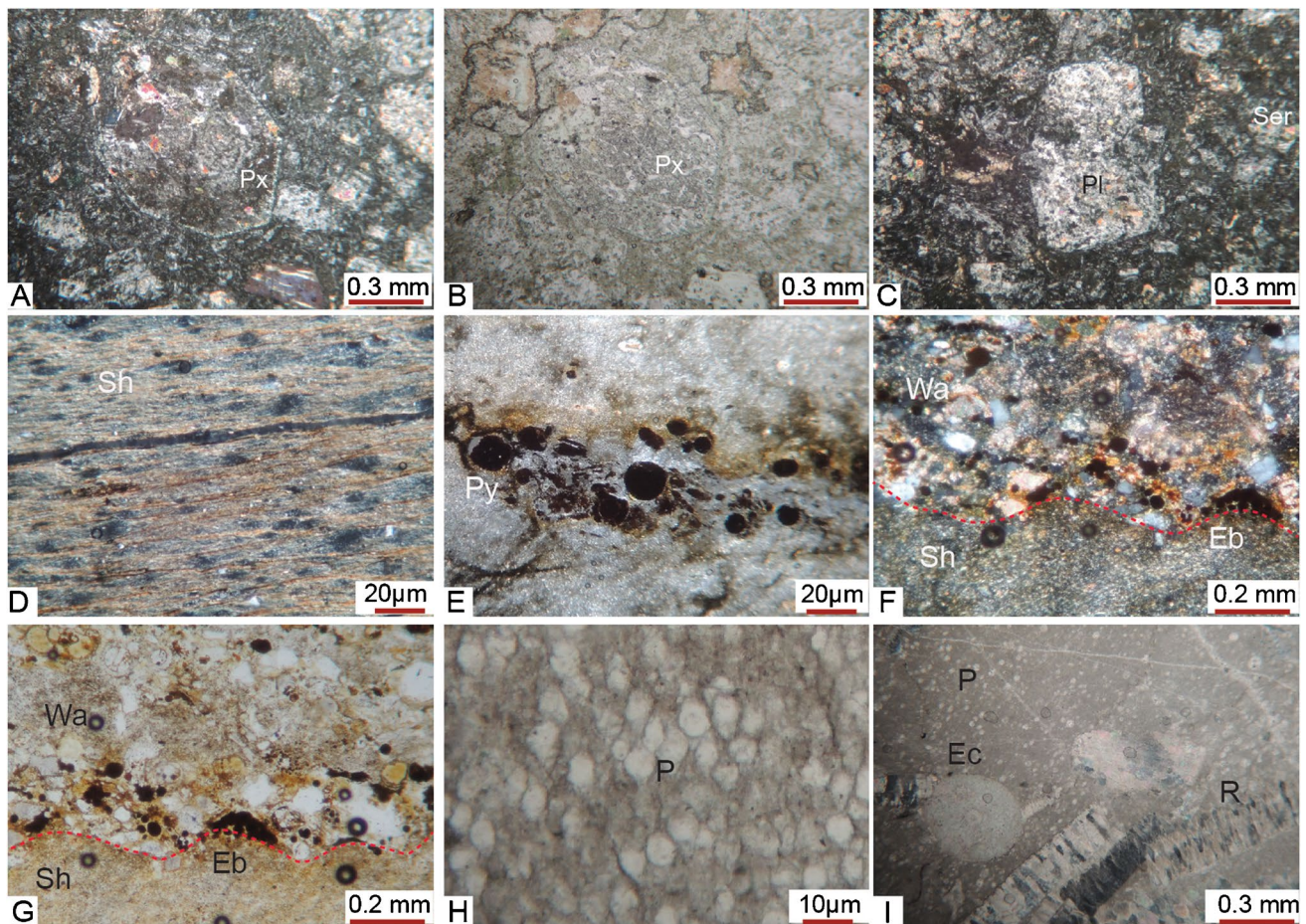


**Fig. 3** (A, B) Micrograph of porphyritic andesite, showing large crystals of clinopyroxene (Px), plagioclase, and amphibole (A) XPL and (B) PPL. (C) Coarse grain plagioclase (Pl) with locally altered to sericite (Ser), XPL. (D) Micrograph of the gray shale (Sh) showing the occurrence of detrital quartz, mica, pyrite, and iron oxide, XPL. (E) Micrograph of the gray shale, including pyrite (Py), PPL.

(F, G) Lithicwacke (Wa), including quartz, feldspar, chert, and carbonate rock fragment. The figures show the erosional boundaries (Eb) between lithicwacke and shale (Sh) facies, (F) XPL, and (G) PPL. (H, I) Micrographs of deep open-marine facies including *Globotruncana* packstone (P) and calciturbidite facies contain echinoid (Ec), rudist (R), and pelagic (P) fauna, XPL

Trace element compositions were determined by inductively coupled plasma–mass spectrometry (ICP–MS), Agilent 7700×. The isotope ratios of Sr were measured using thermal ionization mass spectrometers (TIMS), VG Sector 54–30, and were corrected for fractionation based on  $^{86}\text{Sr}/^{88}\text{Sr}=0.1194$ . NIST–SRM987 was adopted as a standard for  $^{87}\text{Sr}/^{86}\text{Sr}$ , and the average and 1SE ( $\pm 1$  sigma error) for the isotope ratio standard are  $^{87}\text{Sr}/^{86}\text{Sr}=0.710244 \pm 0.000009$  ( $n=11$ ).

## Results and discussion

### Rb–Sr whole-rock isochron

Sr isotope ratios and abundance of Rb and Sr for the shale samples are listed in Table 4. The rubidium-strontium isotope system is used to estimate the depositional age of the shale

samples. The  $^{87}\text{Sr}/^{86}\text{Sr}$  ratios vary from 0.7115 to 0.7186 with average of  $=0.7102 \pm 0.0016$ . The Rb–Sr plots show a linear trend. We assumed the linear trend as the Rb–Sr whole-rock isochron and calculated the age and initial ratio:  $125 \pm 39$  Ma with an initial ratio of  $^{87}\text{Sr}/^{86}\text{Sr}=0.7106 \pm 0.0032$  for all the nine samples (Fig. 4A), and  $129 \pm 31$  Ma with an initial ratio of  $^{87}\text{Sr}/^{86}\text{Sr}=0.7104 \pm 0.0014$  for seven samples within a range of  $^{87}\text{Sr}/^{86}\text{Sr}=0.01\%$  difference from the isochron line (Fig. 4B).

Zahedi and Hajian (1985), based on biostratigraphy and stratigraphic position of Sanandaj shale, suggested the ages of the deposition/Sanandaj shale is Upper Cretaceous. In contrast, its depositional age obtained from the Rb–Sr isotope (Compston and Pidgeon 1962) is Lower Cretaceous. This difference demonstrates that Sanandaj shale samples comprise a mixture of grains with variable isotopic compositions inherited from their source regions and authigenic minerals. Therefore, based on whole-rock Rb–Sr isochron age does not show the depositional age of the Sanandaj shale.

**Table 1** Results of major and trace elements compositions for the shale samples from the K8 unit

Sample SH-	1	2	3	4	5	6	7	8	9	Average
Major oxides (wt. %)										
SiO <sub>2</sub>	71/2	79/5	74/5	67/9	72/0	69/7	69/3	74/3	67/5	71/8
SiO <sub>2</sub> *	62/2	58/8	59/7	61/1	59/6	59/5	62.0	64/2	62/4	60/9
TiO <sub>2</sub>	0/71	0/79	0/95	0/90	0/83	0/90	0/80	0/56	0/87	0/81
Al <sub>2</sub> O <sub>3</sub>	16/1	14/6	18/5	19/1	16/1	17/3	17/9	14/2	19/9	17/1
Fe <sub>2</sub> O <sub>3</sub>	4/66	1/67	2/13	5/01	5/55	5/33	6/16	5/19	7/44	4/79
MnO	0/09	0/00	0/00	0/00	0/01	0/00	0/01	0/05	0/01	0/02
MgO	2/26	0/76	0/84	1/88	1/19	1/83	1/55	1/58	1/28	1/46
CaO	0/76	0/17	0/21	0/28	0/20	0/18	0/43	0/23	0/26	0/30
Na <sub>2</sub> O	1/80	1/67	2/04	1/12	1/86	1/84	1/92	1/16	1/89	1/70
K <sub>2</sub> O	2/45	2/68	3/45	3/82	2/56	3/08	3/47	2/62	3/47	3/07
P <sub>2</sub> O <sub>5</sub>	0/03	0/02	0/04	0/08	0/07	0/04	0/08	0/04	0/06	0/05
LOI	4/33	3/65	3/51	4/94	4/50	3/76	4/99	3/89	4/99	4/29
Trace elements (ppm)										
Sc	14/4	10/0	8/5	12/8	8/8	22/7	5/9	11/5	12/9	12/0
V	102	94	111	117	109	168	94	92	129	113
Cr	71	59	52	81	67	111	51	53	83	70
Co	3/6	1/4	5/5	4/4	3/0	7/0	3/1	5/2	3/9	4/1
Ni	29	10	31	29	22	51	23	51	32	31
Cu	2/9	2/8	11/5	23/7	5/2	57/2	2/8	49/1	31/9	20/8
Zn	48	29	46	103	53	220	55	97	123	86
Ga	19/6	16/3	21/5	22/0	17/5	32/2	13/0	18/1	23/5	21/6
Rb	36	59	46	55	47	71	35	65	73	54
Sr	84	49	133	79	46	84	27	40	92	70
Y	16/4	6/0	6/7	7/1	3/7	17/5	3/3	9/3	7/1	8/6
Zr	57/0	40/3	47/4	42/8	19/5	78/2	19/1	71/3	47/5	47/0
Nb	7/4	8/7	24/8	9/3	8/0	6/3	5/5	8/5	4/9	9/3
Ba	640	326	566	362	494	707	178	629	535	493
Hf	0/5	0/5	1/4	0/5	0/8	0/4	0/5	0/6	0/3	0/6
Ta	1/9	1/3	1/3	1/1	0/9	1/8	0/9	2/1	1/5	1/4
Pb	1/3	2/2	5/1	8/4	3/5	28/0	2/1	5/9	11/8	7/6
Th	7/5	6/5	5/7	7/2	3/7	10/9	3/8	5/6	7/1	6/5
U	1/1	0/9	0/9	1/1	0/8	1/4	0/6	1/2	1/3	1/0
REEs (ppm)										
La	25/4	19/8	18/1	17/1	4/5	16/3	15/0	15/6	20/8	17/0
Ce	50/8	44/4	41/8	37/4	9/6	31/8	30/2	24/6	44/1	35/0
Pr	5/7	5/0	4/6	4/1	1/2	4/6	3/4	2/8	4/7	4/0
Nd	20/8	18/7	16/5	14/9	4/9	18/2	11/6	9/2	17/6	14/7
Sm	3/7	3/2	2/2	2/4	0/9	3/9	1/5	1/4	3/0	2/5
Eu	1/0	0/6	0/2	0/4	0/1	0/7	0/2	0/1	0/4	0/4
Gd	3/3	2/1	1/1	1/5	0/6	3/5	0/9	1/3	1/6	1/8
Tb	0/5	0/2	0/2	0/2	0/1	0/5	0/1	0/2	0/2	0/2
Dy	3/1	1/2	1/1	1/4	0/7	3/2	0/7	1/6	1/4	1/6
Ho	0/6	0/3	0/2	0/3	0/2	0/7	0/1	0/4	0/3	0/3
Er	1/8	0/7	0/8	0/9	0/5	2/0	0/4	1/2	0/9	1/0
Tm	0/3	0/1	0/1	0/1	0/1	0/3	0/1	0/2	0/2	0/2
Yb	1/6	0/8	0/8	1/0	0/5	2/0	0/4	1/4	1/0	1/0
Lu	0/2	0/1	0/1	0/1	0/1	0/3	0/1	0/2	0/2	0/2

**Table 2** Ratios and computed parameters of the chemical analyses of shale samples from the K8 unit

Sample SH-	1	2	3	4	5	6	7	8	9	Average
Fe <sub>2</sub> O <sub>3</sub> + MgO	6.9	2.4	3.0	6.9	6.7	7.2	7.7	6.8	8.7	6.3
Al <sub>2</sub> O <sub>3</sub> + K <sub>2</sub> O + Na <sub>2</sub> O	20.4	19.0	24.0	24.1	20.5	22.2	23.3	18.0	25.2	21.8
Y + Nb	23.8	14.8	31.5	16.4	11.8	23.8	8.8	17.8	12.0	17.8
Al <sub>2</sub> O <sub>3</sub> /TiO <sub>2</sub>	22.6	18.4	19.5	21.2	19.4	19.2	22.4	25.3	22.8	21.2
K <sub>2</sub> O/Al <sub>2</sub> O <sub>3</sub>	0.15	0.18	0.19	0.20	0.16	0.18	0.19	0.18	0.17	0.18
K <sub>2</sub> O/Na <sub>2</sub> O	1.36	1.61	1.70	3.43	1.38	1.68	1.81	2.25	1.84	1.81
SiO <sub>2</sub> /Al <sub>2</sub> O <sub>3</sub>	4.4	5.4	4.0	3.6	4.5	4.0	3.9	5.2	3.4	4.2
LREEs	107	92	83	76	21	75	62	54	91	74
HREEs	11.4	5.6	4.4	5.7	2.6	12.4	2.8	6.5	5.7	6.3
REEs	119	97	88	82	24	88	65	60	96	80
LREEs/HREEs	9.4	16.4	19.0	13.5	8.1	6.1	22.6	8.2	15.9	11.6
Ba/Th	85.2	49.9	98.8	50.4	134.2	64.8	46.7	111.9	75.3	76.4
Cr/Th	9.4	9.1	9.0	11.2	18.2	10.2	13.3	9.4	11.6	11.3
Cr/V	0.7	0.6	0.5	0.7	0.6	0.7	0.5	0.6	0.6	0.6
Co/Th	0.5	0.2	1.0	0.6	0.8	0.6	0.8	0.9	0.5	0.7
Dy/Yb	1.9	1.5	1.3	1.5	1.5	1.6	1.7	1.1	1.4	1.5
Ga/Rb	0.54	0.28	0.46	0.40	0.37	0.46	0.37	0.28	0.32	0.40
La/Co	7.1	14.0	3.3	3.9	1.5	2.3	4.8	3.0	5.4	5.0
La/Nb	3.4	2.3	0.7	1.8	0.6	2.6	2.7	1.8	4.3	2.2
La/Sc	1.8	2.0	2.1	1.3	0.5	0.7	2.5	1.4	1.6	1.5
La/Sm	6.8	6.2	8.4	7.1	5.1	4.2	9.8	10.9	7.0	7.3
La/Th	3.4	3.0	3.2	2.4	1.2	1.5	4.0	2.8	2.9	2.7
La/Yb	15.6	25.1	22.2	17.6	9.7	8.3	37.7	11.2	20.6	16.2
Nb/La	0.29	0.44	1.37	0.54	1.79	0.39	0.37	0.54	0.24	0.44
Nb/Ta	3.9	6.7	18.5	8.1	8.7	3.5	6.5	4.1	3.4	7.0
Nb/Th	0.99	1.34	4.34	1.29	2.18	0.58	1.45	1.51	0.69	1.44
Sc/Ni	0.49	1.00	0.27	0.45	0.40	0.44	0.26	0.22	0.41	0.39
Ta/Yb	1.2	1.6	1.6	1.2	2.0	0.9	2.1	1.5	1.4	1.5
Th/Co	2.1	4.6	1.0	1.6	1.2	1.6	1.2	1.1	1.8	1.8
Th/Sc	0.5	0.7	0.7	0.6	0.4	0.5	0.6	0.5	0.5	0.5
Th/U	6.5	7.2	6.4	6.8	4.7	7.7	6.0	4.5	5.6	6.2
Th/Yb	4.6	8.3	7.0	7.4	8.0	5.6	9.5	25.2	34.8	12.3
Y/Ho	25.2	20.2	28.1	22.9	24.6	25.9	22.4	24.4	25.0	24.3
Y/Nb	2.21	0.69	0.27	0.77	0.46	2.76	0.61	1.10	1.44	0.92
Y/Ni	0.56	0.60	0.22	0.25	0.17	0.34	0.15	0.18	0.22	0.28
Zr/Hf	106.7	73.9	34.6	84.2	24.5	219.2	35.3	128.6	164.2	77.0
Zr/Nb	7.7	4.6	1.9	4.6	2.4	12.4	3.5	8.4	9.7	6.1
Zr/TiO <sub>2</sub>	80.1	50.8	50.0	47.5	23.4	86.8	23.9	127.4	54.6	57.8
La/Lu <sub>CN</sub>	11.6	16.5	15.8	11.8	5.4	5.8	24.4	7.1	13.8	12.5
La/Yb <sub>CN</sub>	8.8	14.1	12.5	9.9	5.5	4.7	21.2	6.3	11.6	10.5
Nd/Er <sub>CN</sub>	4.3	9.6	7.6	5.8	4.0	3.3	10.8	2.8	7.3	6.2
Ce/Ce* <sub>SN</sub>	0.97	1.03	1.06	1.03	0.93	0.85	0.97	0.85	1.02	0.97
Eu/Eu* <sub>SN</sub>	0.9	0.7	0.5	0.7	0.3	0.6	0.7	0.3	0.7	0.6
Gd/Yb <sub>CN</sub>	1.2	1.6	0.8	0.9	0.8	1.0	1.3	0.5	0.9	1.0
Nb/Nb* <sub>SN</sub>	0.18	0.26	0.82	0.28	0.67	0.16	0.25	0.31	0.14	0.34
CIA	70	71	71	75	72	72	70	73	73	72
CIW	79	83	83	89	82	84	82	86	85	84
CIW'	84	84	85	91	84	85	85	88	86	86
PIA	76	79	80	86	80	81	78	83	82	80
Mn*	-3.6	-6.1	-6.2	-5.1	-4.7	-6.6	-4.9	-3.9	-4.7	-5.1
Ni/Co	8.1	7.1	5.6	6.5	7.3	7.3	7.2	9.9	8.2	7.5
V/Cr	1.5	1.6	2.1	1.5	1.6	1.5	1.8	1.7	1.6	1.7
V/Ni	3.5	9.4	3.6	4.1	4.9	3.3	4.1	1.8	4.1	4.3
V/(V + Ni)	0.78	0.90	0.78	0.80	0.83	0.77	0.81	0.64	0.80	0.79

Eu/Eu\* = [2\*Eu/(Sm + Gd)]<sub>SN</sub>; Ce/Ce\* = [2Ce/(La + Pr)]<sub>SN</sub>; SN = Post Archean Australian Shale; Nb/Nb\* = [Nb/(Th\* La)<sup>0.5</sup>]<sub>CN</sub>; CN: Chondrite-normalized; SiO<sub>2</sub>\* = 39.34 + 1.2578 (Al<sub>2</sub>O<sub>3</sub>/TiO<sub>2</sub>) - 0.0109 \*(Al<sub>2</sub>O<sub>3</sub>/TiO<sub>2</sub>)<sup>2</sup>; CIA = [Al<sub>2</sub>O<sub>3</sub>/(Al<sub>2</sub>O<sub>3</sub> + CaO\* + Na<sub>2</sub>O)]\*100; CIW = [Al<sub>2</sub>O<sub>3</sub>/(Al<sub>2</sub>O<sub>3</sub> + K<sub>2</sub>O + Na<sub>2</sub>O + CaO\*)\*100]; CIW' = [Al<sub>2</sub>O<sub>3</sub>/(Al<sub>2</sub>O<sub>3</sub> + Na<sub>2</sub>O)]\*100; PIA = [(Al<sub>2</sub>O<sub>3</sub>-K<sub>2</sub>O)/(Al<sub>2</sub>O<sub>3</sub> + CaO\* + Na<sub>2</sub>O-K<sub>2</sub>O)]\*100; Mn\* = Log [(Mn<sub>sample</sub>/Mn<sub>shale</sub>)/(Fe<sub>sample</sub>/Fe<sub>shale</sub>)]; Fe<sub>shale</sub> = 6\*10<sup>-4</sup>; Mn<sub>shale</sub> = 4.6\*10<sup>-2</sup>; CaO\* refers to the mole fraction CaO in silicate minerals

**Table 3** Pearson's correlation coefficients among elements, indices, and some elemental ratios from the UCS samples

	SiO <sub>2</sub>	TiO <sub>2</sub>	Al <sub>2</sub> O <sub>3</sub>	Fe <sub>2</sub> O <sub>3</sub>	MnO	MgO	CaO	Na <sub>2</sub> O	K <sub>2</sub> O	P <sub>2</sub> O <sub>5</sub>	LOI	Sc	V	Cr	Co	Ni	Rb	Cs	Sr	Zr			
SiO <sub>2</sub>	1																						
TiO <sub>2</sub>	-0.31	1																					
Al <sub>2</sub> O <sub>3</sub>	-0.74*	0.75*	1																				
Fe <sub>2</sub> O <sub>3</sub>	-0.83**	-0.10	0.39	1																			
MnO	0.01	-0.72*	-0.42	0.12	1																		
MgO	-0.60	-0.27	0.06	0.48	0.60	1																	
CaO	-0.27	-0.32	-0.01	0.18	0.80**	0.67*	1																
Na <sub>2</sub> O	-0.09	0.46	0.27	-0.03	-0.15	-0.32	0.11	1															
K <sub>2</sub> O	-0.55	0.66	0.87**	0.20	-0.60	-0.05	-0.22	-0.02	1														
P <sub>2</sub> O <sub>5</sub>	-0.71*	0.30	0.58	0.63	-0.35	0.17	-0.05	-0.11	0.60	1													
LOI	-0.77*	0.09	0.54	0.76*	0.00	0.37	0.32	-0.10	0.43	0.82**	1												
Sc	-0.29	0.11	0.05	0.18	0.10	0.52	-0.01	-0.10	-0.08	-0.32	-0.22	1											
V	-0.48	0.56	0.45	0.29	-0.35	0.23	-0.29	0.22	0.28	0.02	0.09	0.83**	1										
Cr	-0.52	0.40	0.34	0.37	-0.17	0.44	-0.11	0.01	0.16	0.02	0.09	0.90**	0.92**	1									
Co	-0.36	0.19	0.27	0.17	-0.04	0.34	-0.18	-0.07	0.26	-0.03	-0.28	0.63	0.67*	0.50	1								
Ni	-0.32	-0.22	0.01	0.36	0.21	0.45	-0.11	-0.27	0.02	-0.09	-0.21	0.63	0.51	0.42	0.90**	1							
Rb	-0.05	0.05	0.06	0.20	-0.33	-0.15	-0.64	-0.28	0.10	-0.19	-0.18	0.57	0.56	0.55	0.37	0.49	1						
Cs	-0.35	0.61	0.48	0.08	-0.46	0.07	-0.45	0.13	0.43	-0.003	-0.25	0.69*	0.91**	0.73*	0.83**	0.60	0.56	1					
Sr	-0.13	0.60	0.55	-0.26	-0.10	-0.07	-0.01	0.31	0.36	-0.24	-0.28	0.30	0.45	0.28	0.49	0.19	0.12	0.61	1				
Zr	0.03	0.25	-0.18	-0.05	0.31	0.38	-0.03	-0.29	-0.17	-0.58	-0.51	0.79	0.48	0.48	0.71*	0.80**	0.57	0.54	0.35	1			
Hf	0.39	0.27	0.02	-0.57	-0.16	-0.49	-0.20*	0.29	0.05	-0.11	-0.48	-0.43	-0.22	-0.50	0.18	-0.08	-0.38	-0.10	0.47	0.17	1		
Th	-0.20	0.23	0.15	-0.002	-0.1	-0.41	-0.01	-0.07	0.07	-0.41	-0.28	0.95**	0.78	0.84*	0.56	0.50	0.56	0.70*	0.45	0.78	0.47	1	
U	-0.28	-0.04	0.11	0.26	0.16	0.39	-0.11	-0.29	-0.01	-0.32	-0.16	0.86	0.66	0.73	0.61	0.71*	0.77*	0.61	0.39	0.86	0.45	0.78	1
Fe <sub>2</sub> O <sub>3</sub> +MgO	-0.86	-0.15	0.36	0.98**	0.25	0.66	0.31	-0.11	0.17	0.58	0.74	0.28	0.31	0.43	0.24	0.43	0.14	0.10	-0.24	-0.52	-0.05	-0.05	1
K <sub>2</sub> O/Al <sub>2</sub> O <sub>3</sub>	-0.04	0.35	0.34	-0.20	-0.65	-0.22	-0.48	-0.34	0.76	0.33	-0.004	-0.16	0.04	-0.10	0.24	0.07	0.14	0.31	0.07	-0.05	-0.05	-0.05	1
LREEs	0.04	0.12	0.22	-0.28	0.25	0.17	0.43	0.11	0.15	-0.51	-0.13	0.30	0.10	0.17	-0.01	-0.09	0.05	0.78	0.52	0.38	0.38	0.82**	1
HREEs	-0.06	-0.12	-0.14	-0.01	0.45	0.63	0.35	-0.06	-0.28	-0.54	0.32	0.89**	0.55	0.66	-0.49	0.53	0.27	0.42	0.30	0.82**	0.82**	0.82**	1
REEs	0.08	0.11	0.19	-0.26	0.29	0.25	0.45	0.11	0.11	-0.54	-0.16	0.39	0.17	0.25	0.06	-0.01	0.07	0.13	0.52	0.45	0.45	0.45	1
L/HREEs	-0.04	0.32	0.42	-0.18	-0.38	-0.46	0.02	0.32	0.58	0.26	0.24	-0.68*	-0.40	-0.54	-0.39	-0.55	-0.36	-0.27	-0.05	-0.57	-0.57	-0.57	1
Th/Sc	-0.46	0.30	0.11	-0.72	0.38	-0.47	-0.16	0.04	0.41	-0.26	-0.34	-0.33	-0.27	-0.39	-0.17	-0.40	-0.4915	-0.03	0.27	-0.11	-0.11	-0.11	1
Th/U	0.03	0.52	0.21	-0.41	-0.28*	-0.12	0.04	0.16	0.27	-0.31	-0.27	0.50	0.48	0.49	0.15	-0.11	0.07	0.40	0.47	0.26	0.26	0.26	1
Zr/Hf	-0.31	-0.07	0.08	0.37	0.11	0.42	-0.07	-0.14	-0.02	-0.30	-0.11	0.89**	0.72*	0.78	0.56	0.69	0.76*	0.59*	-0.19	0.82**	0.82**	0.82**	1
Ce/Ce <sup>SN</sup>	0.08	0.52	0.49	-0.37	-0.29	-0.42	0.07	0.22	0.48	0.09	0.18	-0.48	-0.28	-0.21	-0.46	-0.70	-0.28	-0.18	0.44	-0.49	-0.49	-0.49	1
Eu/Eu <sup>SN</sup>	-0.25	0.2	0.33	-0.003	0.22	0.38	0.64	0.17	0.22	-0.11	0.30	0.20	-0.07	0.24	-0.25	-0.33	-0.23	-0.11	-0.21	-0.003	-0.003	-0.003	1
ClA	-0.36	0.12	0.29	0.30	-0.30	0.12	-0.46	-0.71*	0.41	-0.39	0.28	0.25	-0.28	0.37	0.29	0.33	0.60	-0.36	0.08	0.21	0.21	0.21	1
ClW	-0.25	0.14	0.30	0.16	0.46	-0.01	-0.57	-0.71*	0.58	0.37	0.19	0.15	0.21	0.23	0.31	0.32	0.60	0.38	0.04	0.21	0.21	0.21	1
ClW'	-0.38	-0.03	0.29	0.22	-0.13	0.31	-0.18	-0.83	0.54	0.44	0.34	0.08	0.03	0.12	0.30	0.33	0.29	0.19	0.02	0.19	0.19	0.19	1
PIA	-0.30	0.16	0.31	0.22	-0.42	0.17	-0.57	0.69	0.51	0.40	0.19	0.18	0.27	0.28	0.37	0.38	0.60	0.42	0.09	0.22	0.22	0.22	1



Table 3 (continued)

	Hf	Th	U	Fe <sub>2</sub> O <sub>3</sub> +MgO	K <sub>2</sub> O/Al <sub>2</sub> O <sub>3</sub>	LREEs	HREEs	REEs	L/HREEs	Th/Sc	Th/U	Zr/Hf	Ce/Ce* <sub>SN</sub>	Eu/Eu* <sub>SN</sub>	CIA	CIW	CIW'	PIA	
Hf	1																		
Th	0.38*	1																	
U	-0.40	0.83	1																
Fe <sub>2</sub> O <sub>3</sub> +MgO	-0.60	0.10	0.32	1															
K <sub>2</sub> O/Al <sub>2</sub> O <sub>3</sub>	0.18	-0.01	0.14	0.22	1														
LREEs	0.19	0.55	0.35	-0.20	-0.03	1													
HREEs	-0.38	0.88	0.74	0.16	0.32	0.53	1												
REEs	-0.22	0.62*	0.41	-0.17*	-0.07	0.99**	-0.62	1											
L/HREEs	0.23	-0.45	-0.61	-0.26	0.49	0.25	-0.60	0.15	1										
Th/Sc	0.36	-0.03	-0.32	-0.73*	0.64	0.49	-0.21	0.42	0.71*	1									
Th/U	-0.15	0.70*	0.20	-0.32	0.28	0.63	0.53	0.66	0.11	-0.52	1								
Zr/Hf	-0.59	0.85**	0.92**	0.42	-0.12	0.34	0.77*	0.41	-0.51	-0.32	0.30	1							
Ce/Ce* <sub>SN</sub>	0.30	-0.23	-0.36	-0.43	0.24	0.46	-0.42	0.37	0.72	0.65	0.25	0.49	1						
Eu/Eu* <sub>SN</sub>	-0.44	0.39	0.07	-0.09	-0.08	0.82*	-0.41	0.82*	0.32	0.31	0.65	0.18	0.45	1					
CIA	-0.21	0.21	0.50	0.29	0.39	-0.20	-0.06	-0.20	-0.30	0.19	-0.14	0.30	0.04	-0.27	1				
CIW	-0.16	0.18	0.38	0.14	0.69*	-0.13	-0.15	-0.15	-0.03	0.12	-0.02	0.25	0.02	-0.24	0.92**	1			
CIW'	-0.16	0.11	0.31	0.27	0.60	0.05	-0.07	-0.06	-0.05	0.06	-0.08	0.14	0.03	-0.08	0.86**	0.90**	1		
PIA	-0.10	0.17	0.43	0.20	0.58	-0.23	-0.14	-0.24	-0.17	-0.03	-0.11	0.25	-0.04	-0.34	0.970**	0.98**	0.88**	1	

\*Correlation is significant at the 0.05 level (2-tailed)

\*\*Correlation is significant at the 0.01 level (2-tailed)

**Table 4**  $^{87}\text{Rb}/^{86}\text{Sr}$ – $^{87}\text{Sr}/^{86}\text{Sr}$  data for the UCS samples

Sample no	Rb	Sr	Rb/Sr	$^{87}\text{Rb}/^{86}\text{Sr}$	$^{87}\text{Sr}/^{86}\text{Sr}$ 2SE
SH-1	36.4	83.8	0.43	1.26	$0.713171 \pm 11$
SH-2	59.3	49.4	1.20	3.48	$0.717206 \pm 14$
SH-3	46.4	133	0.35	1.01	$0.711467 \pm 13$
SH-4	55.5	78.73	0.70	2.04	$0.716593 \pm 14$
SH-5	47.4	45.8	1.03	2.99	$0.715098 \pm 16$
SH-6	70.7	84.3	0.84	2.43	$0.718594 \pm 14$
SH-7	35.5	26.6	1.33	3.86	$0.717946 \pm 14$
SH-8	65.4	40.3	1.62	4.70	$0.717881 \pm 16$
SH-9	72.9	91.9	0.79	2.14	$0.714566 \pm 13$

## Geochemistry

Table 3 represents the concentrations of major and trace elements, elemental ratios, and chemical index of weathering for the nine UCS shale samples. The samples fall in the shale and wacke fields on the log  $\text{Fe}_2\text{O}_3/\text{K}_2\text{O}$  versus log  $\text{SiO}_2/\text{Al}_2\text{O}_3$  chemical classification diagram (Fig. 5A; Heron 1988). The geochemistry of fine-grained clastic sedimentary rocks (Kasanzu et al. 2008) is a powerful tool for studying source rocks, tectonic settings, paleoclimate, and geodynamic evolution of the sedimentary basin (e.g., Dinelli et al. 1999; Zhai et al. 2018).

## Chemical compositions, elemental ratio, and inter-elemental correlations

The major element oxides in the Sanandaj shale samples show inverse linear trends with  $\text{SiO}_2$  (Table 3).  $\text{K}_2\text{O}/\text{Al}_2\text{O}_3$  ratio in sediment is an indicator of the source rocks. This ratio in clay (0.0–0.3) and feldspar (0.3–0.9) minerals are different, and these ratios for the samples vary from 0.15 to 0.20, highlighting the dominance of clay minerals (Cox et al. 1995).

Weak correlations between  $\text{Fe}_2\text{O}_3 + \text{MgO}$  and  $\text{TiO}_2$  ( $r = -0.15$ ),  $\text{K}_2\text{O}$  ( $r = 0.17$ ), high positive correlations between  $\text{Al}_2\text{O}_3$  and  $\text{K}_2\text{O}$  ( $r = 0.87$ ),  $\text{TiO}_2$  ( $r = 0.75$ ) (e.g., Dabard 1990; Condie et al. 1992) associated with  $\text{K}_2\text{O}/\text{Al}_2\text{O}_3$  ratios varying from 0.15 to 0.20 in shales reflecting a higher proportion of aluminosilicates relative to accessory minerals, and clay minerals control the distributions of  $\text{Al}_2\text{O}_3$ ,  $\text{TiO}_2$ , and  $\text{K}_2\text{O}$  (e.g., McLennan et al. 1983; Armstrong-Altrin et al. 2021). The strong correlation between  $\text{K}_2\text{O}$  and  $\text{Al}_2\text{O}_3$  ( $r = 0.87$ ) indicates that samples were affected by post-depositional K-metasomatism (e.g., Fedo et al. 1997; Dey et al. 2008). This process has resulted in a weak positive correlation between  $\text{Al}_2\text{O}_3$  and CIA ( $r = 0.29$ ), and the lack of accurate depositional age determinations of shale samples with the Rb–Sr isotope method.

A weak positive correlation of  $\text{Fe}_2\text{O}_3 + \text{MgO}$  and  $\text{Al}_2\text{O}_3$  ( $r = 0.36$ ) exhibits ferromagnesian minerals (e.g., biotite and chlorite). The high content of  $\text{Fe}_2\text{O}_3$  (an average of 4.8 wt.%)

**Fig. 4**  $^{87}\text{Sr}/^{86}\text{Sr}$ – $^{87}\text{Rb}/^{86}\text{Sr}$  plots for the UCS samples: (A) for nine samples and (B) for seven samples

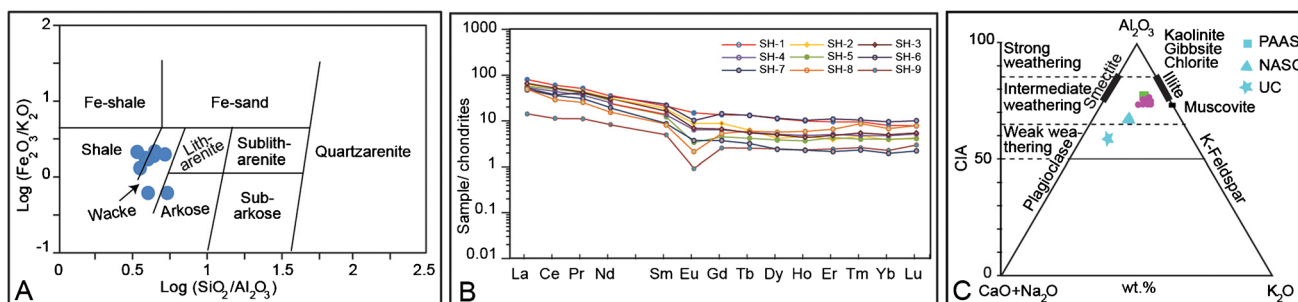
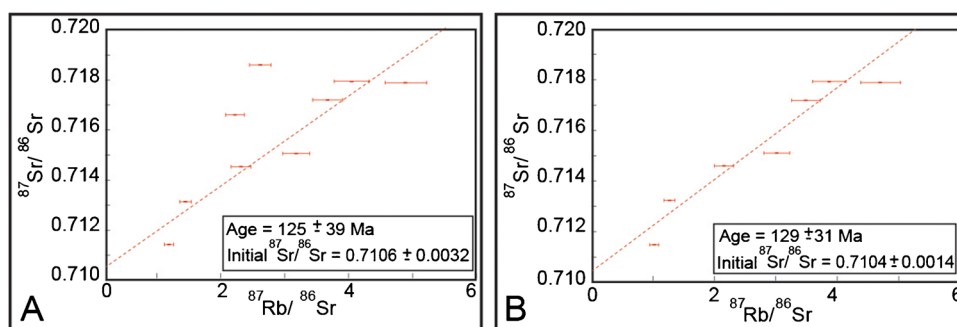


**Fig. 5** (A) Chemical classification of the UCS samples (after Heron 1988). (B) The REE patterns of the UCS shale samples. Data for chondrite-normalization is from Taylor and McLennan (1985). (C)

A-CN-K ( $\text{Al}_2\text{O}_3$ - $\text{CaO}^* + \text{Na}_2\text{O}$ - $\text{K}_2\text{O}$ ) diagram with the associated CIA for the UCS shale samples. The samples fall within the intermediate weathering field (after Nesbitt and Young 1982)

indicates that a part of the  $\text{Fe}_2\text{O}_3$  exists as an oxide/pyrite (e.g., Pettijohn et al. 1987). This interpretation is supported by the linear correlation between  $\text{Fe}_2\text{O}_3$  and LOI ( $r=0.76$ ) and the presence of pyrite observed in thin sections and hand-piece samples (Fig. 3B).

Although no correlation between  $\text{Al}_2\text{O}_3$  and  $\text{MgO}$  ( $r=0.06$ ),  $\text{CaO}$  ( $r=-0.01$ ), and a moderate correlation between  $\text{MgO}$  and  $\text{CaO}$  ( $r=0.67$ ) probably indicates the presence of dolomite. The positive linear correlations between LOI and  $\text{P}_2\text{O}_5$  ( $r=0.82$ ),  $\text{Al}_2\text{O}_3$  ( $r=0.54$ ),  $\text{Fe}_2\text{O}_3$  ( $r=0.76$ ), and  $\text{K}_2\text{O}$  ( $r=0.43$ ), and a high negative correlation of LOI- $\text{SiO}_2$  ( $r=-0.77$ ) show glauconite, phosphate, and pyrite minerals in the samples. These minerals commonly form in a starved basin under anoxic/reducing conditions.

The large-ion lithophile elements (LILs: Rb, Cs, Ba, Sr), Th, and U concentrations are high in the terrigenous rocks. The rubidium concentrations in the samples range from 35 to 73 ppm. Linear correlations of Rb with  $\text{Al}_2\text{O}_3$  ( $r=0.06$ ),  $\text{K}_2\text{O}$  ( $r=0.1$ ), and Sr ( $r=0.12$ ) indicate that Rb neither participates in the same host minerals with Sr nor contributes to K-bearing aluminosilicate minerals. The correlation coefficients of Sr- $\text{Al}_2\text{O}_3$  ( $r=0.55$ ), Sr- $\text{K}_2\text{O}$  ( $r=0.4$ ), and Sr- $\text{CaO}$  ( $r=0$ ) show Sr partly concentrated on aluminosilicate minerals such as illite and mica.

Correlations of U-Th ( $r=0.83$ ), U-LOI ( $r=-0.16$ ), Th-LOI ( $r=-0.28$ ), U- $\text{Al}_2\text{O}_3$  ( $r=0.11$ ), and Th- $\text{Al}_2\text{O}_3$  ( $r=0.15$ ) reveal that U and Th have had similar geochemical behavior during weathering and erosion (e.g., McLennan et al. 1980), and their concentrations are independent of aluminosilicate minerals and organic matter in the samples. The strong correlation between Th and U suggests that they accumulated together in a stable mineral derived from the source rocks and, thus, are not fractionated during sedimentary processing and diagenesis (e.g., Kremer and Tishin 2017; Armstrong-Altrin et al. 2017, 2018).

HFSEs (Zr, Hf, Y, Nb, Ta) are abundant in the felsic upper continental crust (UCC; Taylor and McLennan 1985; McLennan 2001) rather than in mafic rocks. Zirconium and Hf have similar geochemical behaviors and are mainly concentrated in zircon (Bau 1996). The samples contain 0.36–1.37 ppm Hf and 19.1–78.2 ppm Zr and show a weak negative linear correlation between Zr and Hf ( $r=-0.17$ ). The Zr/Hf ratios in the samples range from 25 to 107, which are probably related to changes in a geodynamic setting (e.g., Kremer and Tishin 2017) and subduction processes (e.g., Rudnick et al. 2000).

Linear correlations of U-Zr ( $r=0.86$ ), Th-Zr ( $r=0.78$ ), and weak correlations of U- $\text{Al}_2\text{O}_3$  ( $r=0.11$ ), Th- $\text{Al}_2\text{O}_3$  ( $r=0.15$ ), U- $\text{TiO}_2$  ( $r=-0.04$ ), and Th- $\text{TiO}_2$  ( $r=0.23$ ) indicate that zircon controls the distributions of U and Th. A moderate negative correlation of Zr- $\text{P}_2\text{O}_5$  ( $r=-0.58$ ), U- $\text{P}_2\text{O}_5$  ( $r=-0.32$ ), and Th- $\text{P}_2\text{O}_5$  ( $r=-0.41$ ) represents that phosphate precipitated in the sediments during a slow rate of terrigenous deposits.

Scandium, Cr, V, Co, and Ni are compatible elements and are enriched in mafic to ultramafic rocks during igneous fractionation processes (Dimalanta et al. 2013). Cobalt and Sc in the samples show moderate-to-strong positive correlations with Cr ( $r=0.50$ ;  $r=0.90$ ), Ni ( $r=0.90$ ;  $r=0.63$ ), and V ( $r=0.67$ ;  $r=0.83$ ), whereas they have weak-to-no linear correlations with  $\text{Al}_2\text{O}_3$  ( $r=0.27$ ;  $r=0.05$ ). These characteristics reveal that Co and Sc are concentrated, in part, in oxides and other accessory non-aluminosilicate minerals. Correlation coefficients of V- $\text{TiO}_2$  ( $r=0.56$ ), V- $\text{Al}_2\text{O}_3$  ( $r=0.45$ ), V- $\text{K}_2\text{O}$  ( $r=0.28$ ), and V-LOI ( $r=-0.07$ ) highlight that vanadium is partly hosted in aluminum silicate and not in the organic materials. The samples have relatively low values of Cr (51–111 ppm), Ni (10–51 ppm), and Cr/Ni ratios (1.03–5.88 with an average of 2.65) and show moderate-to-weak linear correlations of Cr-Ni ( $r=0.42$ ), Cr- $\text{Al}_2\text{O}_3$  ( $r=0.34$ ), and no correlation between Ni and  $\text{Al}_2\text{O}_3$  ( $r=0.01$ ). These features may represent a minor contribution of mafic igneous rocks to the depositional system (e.g., Garver and Scott 1995; Armstrong-Altrin et al. 2021).

The samples show LREE/HREE > 1, flat HREE (an average of  $\text{Gd/Yb}_{\text{CN}} = 1$ ), and distinctive negative Eu anomaly (0.26–0.89), indicating derivation from intermediate-acidic rocks in the active continental margin (Taylor and McLennan 1985) (Fig. 5B). The weak-to-no correlation between either  $\text{Al}_2\text{O}_3$  ( $r=0.30$ ) or Zr with Eu/Eu\* ( $r=0.03$ ) reflects that neither clay nor zircon does not play a role in the Eu anomaly.

The lack of correlations between HREEs, LREEs, and REEs with  $\text{Al}_2\text{O}_3$ ,  $\text{TiO}_2$ , and  $\text{P}_2\text{O}_5$  confirms that apatite, monazite/rutile/titanite are not REEs host minerals in the samples. A strong correlation of Zr and LREEs ( $r=0.82$ ) and a weak correlation between Zr-LREEs ( $r=0.38$ ) indicate that zircon is host HREE in shale samples.

Therefore, these rocks were dominantly derived from intermediate-acidic rocks in an active continental margin and deposited in a sediment-starved basin under reducing conditions. They have been affected by post-depositional K-metasomatism.

### Source-area weathering

Geochemical data of the fine-grained sedimentary rocks are significant in determining the weathering intensity of their source rocks (e.g., Lee 2002). Various chemical weathering indices have been proposed based on the molecular percentages of major oxide elements (e.g., Taylor and McLennan 1985). Nesbitt and Young (1982) proposed the CIA as a proxy for chemical weathering in the sediment source area as follows:

$$\text{CIA} = \text{Al}_2\text{O}_3 / (\text{Al}_2\text{O}_3 + \text{K}_2\text{O} + \text{Na}_2\text{O} + \text{CaO}^*) * 100$$

In the equation,  $\text{CaO}^*$  refers to the mole fraction of CaO in silicate minerals. Here, it is less than  $\text{Na}_2\text{O}$ , and the value of CaO remains unchanged (McLennan 1993).

CIA values of the samples range from 70 to 75, with an average of 73, representing moderately weathered source rocks (Table 3). Price and Velbel (2003) suggested that eroded metasediments would have high CIA (65–88) even without further chemical weathering. The samples fall nearby muscovite/illite minerals in the triangle  $\text{Al}_2\text{O}_3$ –( $\text{CaO}^* + \text{Na}_2\text{O}$ )– $\text{K}_2\text{O}$  diagram (Fig. 5C). The locations of samples indicate a moderate-degree alteration of the source rock or low-grade metamorphism of the Sanandaj shale. Table 3 shows weathering intensity indices: CIW (=79–89; Harnois 1988), CIW' (=84–91; Cullers 2000), and PIA (=76–86; Fedo et al. 1995). Strong linear correlations among weathering indices (Table 3), the weak relationship between them with  $\text{Al}_2\text{O}_3$ , and the presence of sericite, are indicating the Sanandaj shale, experienced low-grade metamorphic conditions.

The Rb/Sr ratio is also a significant parameter in identifying the degree of source-rock weathering (McLennan et al. 1993). The shale samples have Rb/Sr ratios from 0.35 to 1.62 with an average of 0.92, which is higher than that calculated for Rb/Sr in the UCC (0.33) and the PAAS (0.80; McLennan et al. 1983). These values show relatively low maturity (e.g., Cisterna et al. 2018) and a moderate weathering intensity in the source area.

Weathering, leaching, and sedimentary recycling lead to the removal of U, whereas the Th content remains constant and the Th/U ratio increases. An average value of Th/U (=4.5–7.7) for the samples is about 6.2, which points to intense weathering and recycling of the source rocks (McLennan et al. 1993). Linear correlations of Th-U ( $r=0.83$ ), Th/U-CIA ( $r=-0.14$ ), Th/U-CIW ( $r=-0.02$ ), Th/U-CIW' ( $r=-0.08$ ), and Th/U-PIA ( $r=-0.11$ ), representing there is no relationship between the Th/U ratios and weathering indices in the samples. That is due to the trapping of uranium and thorium elements in the resistant mineral zircon.

## Source-area paleoclimate

Suttner and Dutta (1986) proposed the binary  $\text{SiO}_2$  against ( $\text{Al}_2\text{O}_3 + \text{K}_2\text{O} + \text{Na}_2\text{O}$ ) diagram to determine the climatic conditions during the deposition of siliciclastic rocks. In this diagram, UCS samples represent arid to semi-arid climates (Fig. 6A). Additionally, the Ga/Rb versus  $\text{K}_2\text{O}/\text{Al}_2\text{O}_3$  diagram (Roy and Roser 2013) for the samples emphasizes the semi-arid climatic conditions (Fig. 6B). The Cretaceous was characterized by humid conditions corresponding to active volcanoes associated with high seafloor spreading rates (Koch and Hansen 2021). Thus, the paleoclimate conditions shown by the samples are probably related to the intense tectonic activity during weathering.

## Sediment recycling

$\text{SiO}_2/\text{Al}_2\text{O}_3$  ratio is an index of sediment maturity and sensitivity to sediment recycling (Roser and Korsch 1986; Armstrong-Altrin et al. 2021).  $\text{SiO}_2/\text{Al}_2\text{O}_3$  ratios for the samples range from 3.4 to 5.4, with an average of 4.3, indicating low sediment maturity (e.g., Roser et al. 1996).

On the Th/Sc–Zr/Sc diagram, the samples follow the general trend of igneous differentiation (Fig. 6C) without indicating sediment recycling. Th/Sc and Zr/Sc values are assumed to remain constant throughout sedimentary processes and represent the original igneous/source rock compositions. In addition, the samples have low Hf (0.29–1.37 < 3–7 ppm) and La/Th ratios (1.22–3.38 < 5), suggesting absence of sediment recycling (e.g., McLennan et al. 1993).

## Source rocks

The source rock is a critical parameter that controls the composition of sedimentary rocks (Taylor and McLennan 1985). Yamamoto et al. (1986) and Willis et al. (1988) suggested that  $\text{Al}_2\text{O}_3/\text{TiO}_2$  ratios of most sedimentary rocks are identical to those of their source rocks. Aluminum and Ti fractionations are insignificant between sediments and their

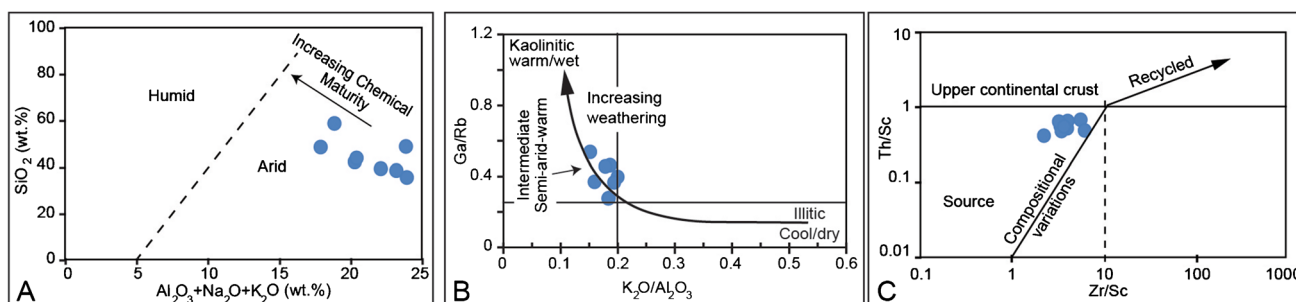


**Fig. 6** (A) Ga/Rb– $\text{K}_2\text{O}/\text{Al}_2\text{O}_3$  diagram for the UCS samples (after Roy and Roser 2013). (B)  $\text{SiO}_2$  vs. ( $\text{Al}_2\text{O}_3 + \text{K}_2\text{O} + \text{Na}_2\text{O}$ ) diagram showing chemical maturity of the UCS samples and their paleocli-

mate (after Suttner and Dutta 1986). (C) Plots of Th/Sc vs. Zr/Sc, monitoring sediment recycling processes for the UCS samples (after McLennan et al. 1993)

parent rocks, but SiO<sub>2</sub> can change during sedimentary rocks' alteration. Hayashi et al. (1997) used Al<sub>2</sub>O<sub>3</sub>/TiO<sub>2</sub> ratios of sedimentary rocks to estimate the SiO<sub>2</sub> content in the source rocks. Poldervaart (1955) and Holland (1984) constructed the following equation for the igneous rocks:

$$\text{SiO}_2^*(\text{wt.}\%) = 39.34 + 1.2578(\text{Al}_2\text{O}_3/\text{TiO}_2) - 0.0109(\text{Al}_2\text{O}_3/\text{TiO}_2)^2$$

The samples contain 58.8 to 64.2 wt.% SiO<sub>2</sub>\* with an average of 60.9 wt.% (based on Al<sub>2</sub>O<sub>3</sub> and TiO<sub>2</sub> values), similar to total SiO<sub>2</sub> in the crust (e.g., Rudnick and Gao 2003), which probably suggests intermediate source rocks. Besides, the Al<sub>2</sub>O<sub>3</sub>/TiO<sub>2</sub> ratios in the samples range from 18.4 to 25.3, with an average of ~21.2, and are equal to those in intermediate and felsic rocks (e.g., Sugisaki 1980; Yamamoto et al. 1986).

Potassium and rubidium are sensitive to sedimentary recycling and are used as indicators of the source rock compositions (Wang et al. 2014). K<sub>2</sub>O versus Rb diagram indicates that samples are generated from intermediate and silicic igneous rocks (Fig. 7A). The samples in K<sub>2</sub>O + Na<sub>2</sub>O versus SiO<sub>2</sub> (LeBas et al. 1986) and SiO<sub>2</sub> versus Zr/TiO<sub>2</sub> (Winchester and Floyd 1977) diagrams show andesite and rhyolite-rhyodacite source rocks, respectively (Fig. 7B, C).

Source rock discrimination diagrams based on major element oxides are sometimes unreliable because some of them, such as alkali and alkaline earth elements, are sensitive to diagenesis. In contrast, the HFSEs and REEs are immobile (e.g., Jian et al. 2013) and resistant to geochemical fractionation during weathering, erosion, and post-depositional processes (Taylor and McLennan 1985; McLennan 1989; Greber and Dauphas 2019). They include both incompatible (Th, La, Hf) and compatible (Sc, Cr, Co) elements whose ratios are significant for separating felsic from mafic source rocks in shales and sandstones (e.g., Cullers 1994; Cox et al. 1995; Fedo et al. 1996). Therefore, their abundances and ratios reflect the features of source rocks (Wang and Zhou 2012; Wang et al. 2012, 2013).

Th/Sc ratio is a sensitive index of source rocks (e.g., McLennan 1989). The felsic and intermediate rocks have Th/Sc ratios of more than 1.0 and 0.6–1.0, respectively (Taylor and McLennan 1985). The Th versus Sc plot (Fig. 7D) shows that shale data cluster below ( $n=5$ ) and above ( $n=4$ ) the Th/Sc=0.6 line, indicating the contribution from intermediate parent rocks.

A typical zircon has a Zr/Hf ratio of ~33.6, which is the average in the crust (Taylor and McLennan 1995). Hafnium content of zircon varies depending on the melt's composition, from which the zircon is crystallized. Ratios of Zr/Hf in the samples (range from 24 to 217) show compositional variation (Table 3), and a comparison with the PAAS illustrates at least exists three types of source rocks in the study area: The ratios are lower than, equal to, and more than that in the

PASS (Zr/Hf=42). Zr/Hf ratios decrease from silica-undersaturated rocks, such as syenite and nepheline syenite (Zr/Hf=60–150) (Correia Neves et al. 1974), to gabbro, diorite, and granitic rocks (Brooks 1970; Cerny et al. 1985). The Zr/Hf ratio can be changed chiefly by mantle metasomatism and partial melting associated with subduction zone processes (e.g., Dostal and Chatterjee 2000).

On the Nb/Th–La/Nb diagram (Wang et al. 2016), the samples lie within arc volcanic rocks or magma fields that may have been polluted by crustal source components (Fig. 7E). La/Nb ratios > 1 ( $n=7$ ) indicate that their source rocks were derived from the lithospheric mantle (Erturk et al. 2018). The samples on the Co/Th versus La/Sc diagram fall close to the felsic volcanic source rocks (Fig. 7F; Cullers 2002).

Bau and Dulski (1996) documented that Y/Ho ratios have nothing relationship with geological processes but rather represent source rocks. Y/Ho ratios range from 20.2 to 28.1 in the samples (Table 3) and correspond to the values of Late Jurassic–Early Cretaceous igneous rocks (20.6 to 26.9) in the study area (Azizi and Asahara 2013). Additionally, in the Cr/V versus Y/Ni diagram (Bailey 1981), all samples fall near the PAAS (Fig. 7G).

Felsic source rocks have high ratios of LREEs/HREEs (> 1), whereas mafic source rocks show lower ratios of LREEs/HREEs (< 1) (Wronkiewicz and Condie 1987). High Nd/Er<sub>CN</sub> (7.5–29.2 > 5) and La/Lu<sub>CN</sub> (5.43–24.4 between 3 and 27) ratios reveal felsic source rocks of samples (e.g., McLennan and Taylor 1991; Cullers 2000).

Eu anomalies are usually inherited from igneous sources in sedimentary rocks (e.g., Taylor and McLennan 1985; McLennan and Taylor 1991). Eu/Eu\* values in samples vary from 0.26 to 0.89. Negative Eu anomaly (Eu/Eu\* < 1) is attributed to the Eu-depleted felsic igneous rocks such as granite and granodiorite in the source region (Taylor and McLennan 1985). The Th/Sc–Eu/Eu\* diagram (Cullers and Podkovyrov 2000) indicates that granodiorite rocks are the predominant sources of samples (Fig. 7H). Eby (1992) noticed that the Y/Nb ratio in granitoid evolved from the crustal melt is > 1.2 and in the mantle melt is < 1.2. Y/Nb ratios of samples range from 0.27 to 2.76 with an average of 1.15, possibly suggesting that source magma was mainly derived from the partial melting of the continental crust. Nb/Ta ratios are 11–12 for the crustal-derived and 17.5 for mantle-derived magma (e.g., Green 1995). The samples have a wide range of Nb/Ta ratios, varying from 3.3 to 18.5 with an average of 7.1, reflecting compositional variation origins due to magma differentiation. Niobium anomalies vary from 0.15 to 0.30 for subduction-related rocks and 0.5 for passive margin sediments (Floyd et al. 1991). Nb/Nb\* anomalies of samples (range from 0.14 to 0.34 except for two with values of 0.66 and 0.82) are mainly consistent with sources derived from subduction-related magmatic rocks (Table 3).

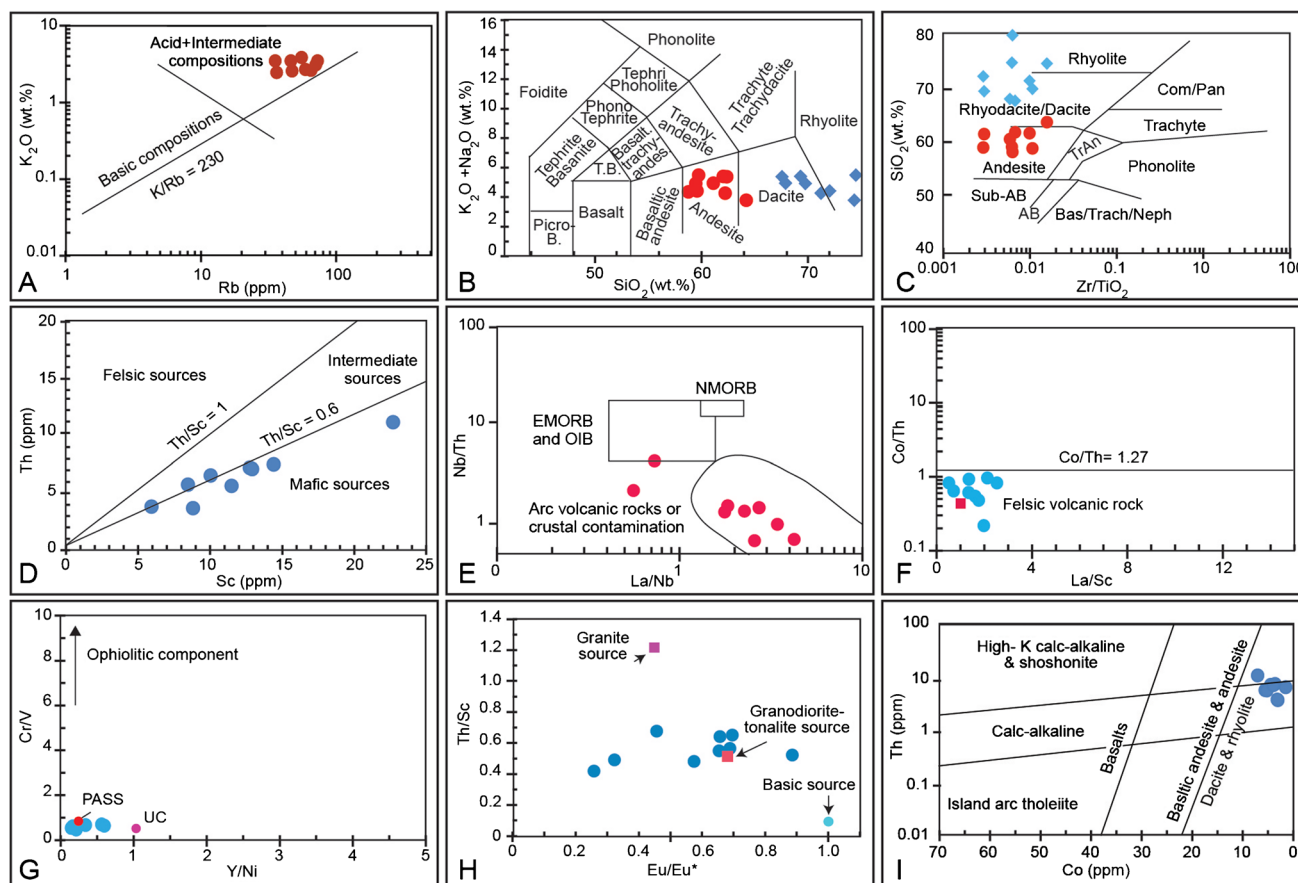


**Fig. 7** (A) Diagram of  $K_2O$  vs. Rb. The main trend of Shaw (1968) with the K/Rb ratio of 230 and the boundary line between acid+intermediate and basic compositions (Floyd and Leveridge 1987) are shown the UCS samples fall in the acid+intermediate field. (B, C) Diagrams of the  $K_2O+Na_2O-SiO_2$  and  $SiO_2-Zr/TiO_2$  (after Winchester and Floyd 1977), based on  $SiO_2^*$  (circle) and  $SiO_2$  (rhomb). (D) Th vs. Sc diagram for the UCS samples. Th/Sc ratios near unity are typical of UCC derivation, and Th/Sc ratios near 0.6 suggest a more mafic component (after Taylor and McLennan 1985). (E) Nb/Th vs. La/Nb plot, showing the UCS samples are derived from arc volcanic rocks or crustal contamination. (F) Discrimination

diagram of Co/Th–La/Sc for the UCS samples (after Gu et al. 2012). Most samples plot below the horizontal line of Co/Th = 1.27, indicating a felsic to an intermediate igneous source. (G) The plot of Cr/V vs. Y/Ni. The arrow points toward an ophiolitic component. The UCS samples plot nearby and below PAAS. PAAS: Post Archaen Australia Shale; UC: Upper Crust. (H) Th/Sc vs. Eu/Eu\* plot (Cullers and Podkovyrov 2000), showing the UCS samples are derived from granodiorite-tonalite. (I) Th–Co classification diagram (Hastie et al. 2007). The UCS samples fall within the calc-alkaline dacite and rhyolite fields

The primitive mantle has  $Zr/Nb = 6.3-7.6$  and  $Nb/La = 1.0$ , and the continental rocks have  $Zr/Nb = 22-25$  and  $Nb/La = 0.46$  (Morata et al. 2005). The negative Nb anomalies ( $= 0.14-0.82$ ), low  $Zr/Nb (= 1.9-12.4)$ , and  $Nb/La (= 0.24-1.79)$  ratios along with  $La/Sm > 4$  of the samples are typical features of arc-related calc-alkaline andesite rocks (e.g., Kelemen et al. 2003) generated in subduction zones (Pearce 1983; Baier et al. 2008). Besides, on the Th–Co diagram (Hastie et al. 2007), the samples plot in calc-alkaline dacite and rhyolite source rock fields (Fig. 7I).

The  $^{87}Sr/^{86}Sr$  ratios for granite and intermediate Jurassic arc rocks in the N-SaSZ are 0.711–0.725 and 0.708, respectively (Shahbazi et al. 2010). The initial  $^{87}Sr/^{86}Sr$  ratio for the shale samples ( $0.7106 \pm 0.0032$ ) is higher and lower than those of the intermediate and felsic source rocks, respectively.

## Tectonic setting

Roser and Korsch (1986) applied the major oxide element patterns ( $K_2O/Na_2O-SiO_2$ ) to discriminate tectonic settings. In this diagram, most samples fall in the active continental margin field and active continental margin-passive margin fields based on the  $SiO_2^*$  and  $SiO_2$  values, respectively (Fig. 8A). The  $SiO_2/Al_2O_3-K_2O/Na_2O$  diagram (Bhatia 1983) suggests that UCS rocks have originated an active continental margin (Fig. 8B). The samples on the Rb/Zr versus Nb and Rb versus Y + Nb diagrams (Peccerillo and Taylor 1976) fall in the normal continental arc (subduction enriched source) and volcanic arc granite fields, too (Fig. 8C, D). In the Th–Sc–Zr/10 and La–Th–Sc triangle diagrams (Bhatia and Crook 1986), samples mainly plot in

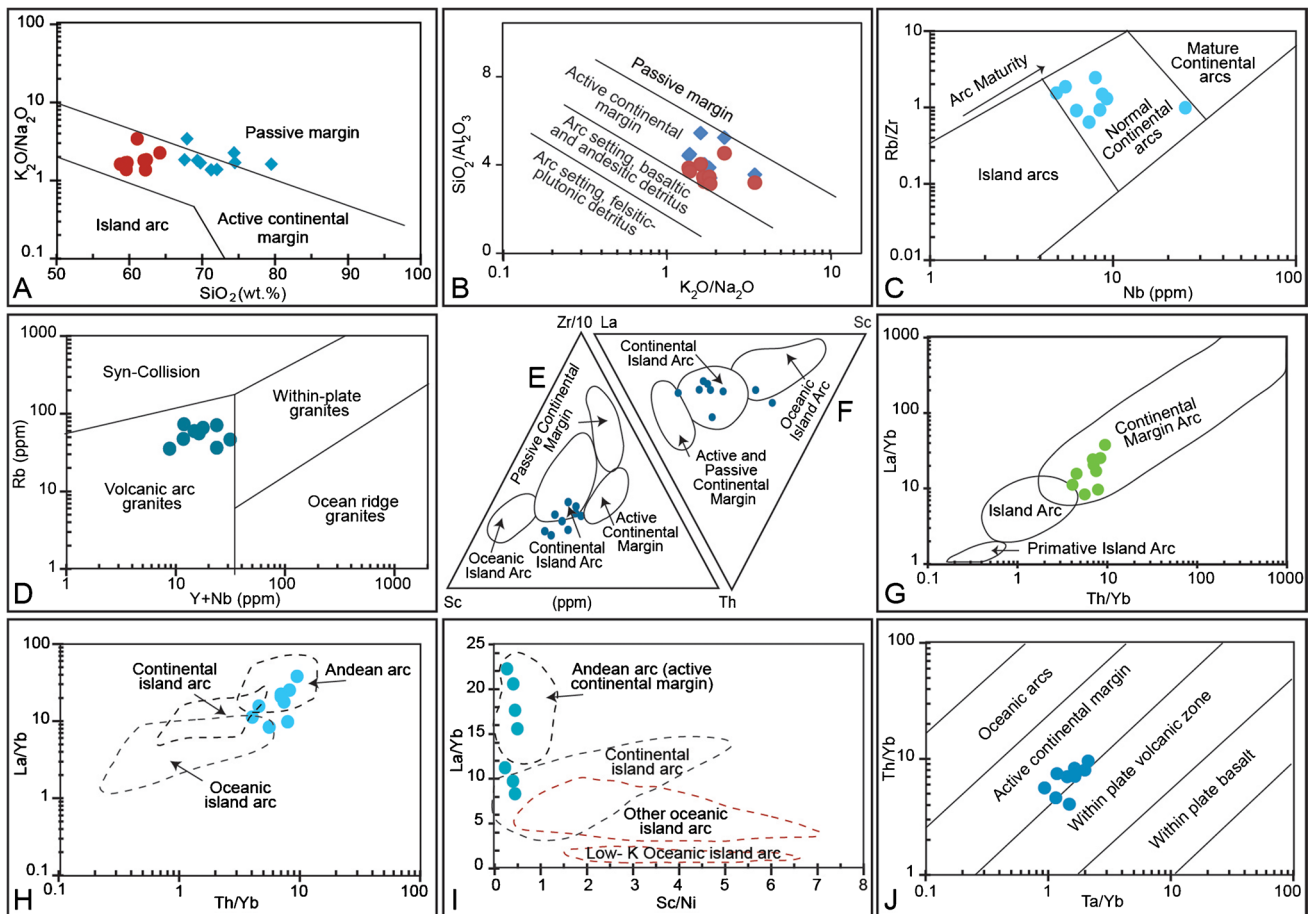


**Fig. 8** (A)  $K_2O/Na_2O$  vs.  $SiO_2$  (circle) and modified  $SiO_2$  (rhomb) plot with discrimination fields (after Roser and Korsch 1986). (B) Diagram of  $SiO_2/Al_2O_3$  vs.  $K_2O/Na_2O$  (after McLennan et al. 1990), samples based on  $SiO_2$  (rhomb) and modified  $SiO_2$  (circle) fall within the ACM area. (C)  $Rb/Zr-Nb$  diagram (Peccerillo and Taylor 1976) represents that samples fall in the normal continental arc field. (D)  $Rb-Y+Nb$  diagram shows that samples plot within the volcanic arc granite field. (E, F)  $Th-Sc-Zr/10$  and  $La-Th-Sc$

diagrams (after Bhatia and Crook 1986). The UCS samples mainly plot within or close to the sectors of continental island arcs and active continental margins. (G)  $La/Yb-Th/Yb$  diagram (Dostal et al. 1996), the UCS samples plot within the sectors of the continental margin arc. (H, I)  $La/Yb-Th/Yb$  (after Condie 1986) and  $La/Yb-Sc/Ni$  (after Bailey 1981) diagrams, the UCS samples mainly show the Andean arc type. (J) The samples on the  $Th/Yb-Ta/Yb$  diagram plot within the active continental margins

the continental island arc (Fig. 8E, F) and on the  $La/Yb-Th/Yb$  diagram (Dostal et al. 1996) fall in the continental margin arc field (Fig. 8G).

Among the arc types, the samples show Andean arc-type geochemical features based on the  $La/Yb-Th/Yb$  (Condie 1986) and  $La/Yb-Sc/Ni$  diagrams (Fig. 8H, I). On the  $Th/Yb$  versus  $Ta/Yb$  diagram (Pearce 1983), samples plot both in the within-plate volcanic zone (WPVZ) and active margin fields (Fig. 8J). The same behavior is observed in complex regions, where volcanic activity is transitional between subduction to extension-related phases (e.g., Gorton and Schandl 2000).

**Paleoredox conditions**

A geochemical index is an effective method to determine the paleoredox conditions during the deposition of mudstone/

shale.  $Mn^*$ , ratios of  $Ni/Co$ ,  $V/V+Ni$ , and  $U/Th$  are sensitive to paleoredox depositional environment conditions (e.g., Rimmer 2004). Manganese is more soluble in anoxic water and would tend to precipitate in overlying/underlying oxygenated waters.  $Mn^*$  value is calculated as follows (e.g., Wedepohl 1978):

$$Mn^* = \log [(Mn_{sample}/Mn_{shales})/(Fe_{sample}/Fe_{shales})],$$

where the values of  $Mn_{shales}$  and  $Fe_{shales}$  are 600 and 46,150 ppm, respectively (Wedepohl 1978).

Negative values of  $Mn^*$  (-3.6 to -6.6) (Table 3) suggest that UCS samples were deposited under reducing conditions (e.g., Brumsack 2006). Besides, the samples show a strong positive correlation between  $Ni$  and  $Co$  ( $r=0.89$ ), high  $Ni/Co$  (5.6-9.9) (> 5: Jones and Manning 1994), and  $V/(V+Ni)$

(0.64–0.90) ratios ( $>0.46$ : Hatch and Leventhal 1992) support the reducing conditions. Meanwhile, low U/Th ratios (0.13 to  $0.22 < 0.75$ ) of the samples highlight that deposition has occurred under oxic conditions (Rogers and Adams 1969), unlike the other proxies. As described before, the strong correlations of Zr-U ( $r=0.86$ ) and Zr-Th ( $r=0.78$ ) indicate that U and Th are hosted in zircon (Bea 1996). The high chemical resistance of zircon leads to the U and Th values being insensitive to redox conditions. Therefore,  $Mn^*$ ,  $V/(V+Ni)$ , and Ni/Co values show dysoxic/anoxic marine conditions.

## Sedimentary environment

The chemical compositions of the UCS samples imply that deposition occurred in an active continental margin environment. This setting is common in the convergent plate boundaries. Active continental margins include trench, trench slope, fore-arc, and back-arc settings (Bailleul et al. 2007). The  $REE_{CN}$  patterns,  $Eu/Eu^*_{SN}$  anomaly, and Rb–Sr isotope system of the shale samples reveal that detritus were derived from the weathering of the young differentiated arc in the subduction zone (e.g., McLennan et al. 1993; Girty et al. 1996). Lithofacies and their stacking patterns of the UCS (Fig. 1C) are comparable to those from the trench (K8 unit) to trench slope (K8 and K9 units) and fore-arc (K8, K10–K12 units) basins (Draut and Clift 2012). Paleoredox indices, slightly negative Ce anomalies (0.85 to 1.03 with an average of 0.97), and the negative linear correlation between  $Ce/Ce^*_{SN}$  and HREEs/LREEs ratio ( $r = -0.72$ ) indicate that shale layers formed predominantly in the clastic sediment-starved basin under reducing conditions (e.g., Rimmer et al. 2004). The volcanic activity may have caused the upwelling of the anoxic deep-water, the demise of planktonic foraminifera, and the deposition of marine black shale-bearing pyrite (Fig. 3G) during the Late Cretaceous (e.g., Schlanger et al. 1987; Ohkouchi et al. 2015). The deposits of these settings are mainly derived from the slope and accumulated in the basin like the turbidites (i.e., flysch deposits) in the northern North Atlantic (e.g., ODP Site 1276; Trabucho-Alexandre et al. 2011) and Mariana Basin (DSDP Site 585; Whitman et al. 1985).

Carbonate facies association with the shale layers represents the warm conditions during deposition (Hay 1981). Due to high relief, no effective recycling occurs in turbidites. These deposits preserve provenance characteristics such as source rocks and the evolution of magmatic and plate tectonic systems (Clift et al. 2000). Therefore, they would be ideal candidates for studying the geodynamic evolution of basins (e.g., Guo et al. 2012).

## Geodynamics

The geodynamic evolution of the SaSZ has been controlled through the opening and later closure of the Neotethys Ocean at the northeastern margin of Gondwana (Alavi 1994). Berberian and King (1981) proposed a new rift roughly at this location of the main Zagros thrust from the Early Permian to the Middle Triassic, resulting in the development of the Neotethys basin. Following that, the Iranian plate was separated from the Arabian plate. From the Late Triassic, the Neotethys oceanic basin was reduced in its extent by subduction oceanic crust (final Wilson cycle stages) beneath the Iranian continental plate. The continued subduction generated an active arc margin and a deep-water trench basin. During the initial phase, the basin was filled with mud and organic matter derived from the water column (because of the lack of a significant source of deposits) associated with submarine volcanic rocks.

On the Ba/Th versus  $^{87}Sr/^{86}Sr$  diagram (Fig. 9), samples fall in the pelagic sediment field/global subducting sediments in the trench, GLOSS (e.g., Plank and Langmuir 1998; Kilian and Behrmann 2003; Özdemir and Güleç 2014). Released fluids from dehydrating of the oceanic slab also resulted in post-depositional K-metasomatism (e.g., Fedo et al. 1997; Dey et al. 2008) and a weak positive correlation between  $Al_2O_3$  and CIA ( $r = 0.29$ ).

Slope instability processes have eroded the accumulated sediments on the slope and re-deposited them in the basin as turbidites. Also, the trench changed to the trench slope and fore-arc basins during the northeastward migration of the arc.

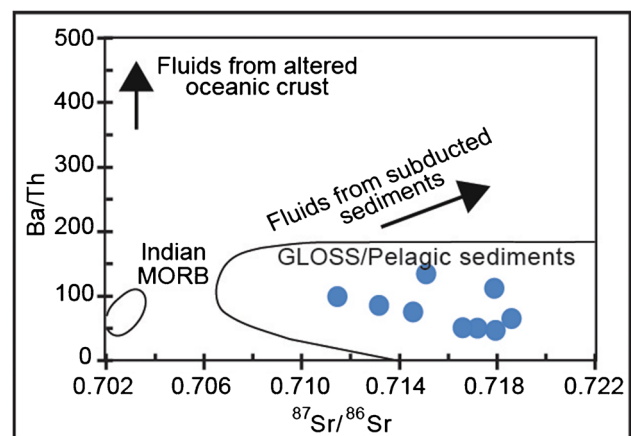


**Fig. 9** Ba/Th vs.  $^{87}Sr/^{86}Sr$  diagram for the UCS samples showing the UCS samples fall within GLOSS (global subducted sediments)/pelagic sediments (Plank and Langmuir 1998)



Black shales can be deposited during most of the Wilson cycle stages, but their properties are dependent on the depositional environment and the Wilson cycle stages. The REE<sub>CN</sub> patterns of the UCS shale are comparable to those found in the UCC, turbidites from the Phanerozoic continental arc, the young differentiated arc type in modern deep-sea (McLennan and Taylor 1991), and REE<sub>S<sub>CN</sub></sub> patterns for Indian sediments (Othman et al. 1989) (Fig. 10A–C).

LREE<sub>CN</sub> enrichment (mean La/Yb<sub>CN</sub> = 10.5), low yttrium (Y < 20 ppm), and Yb concentrations (Yb < 2 ppm) of the samples (Table 3) are similar to adakite (e.g., Kelemen et al. 2003), which originate from melting of the young subducted lithosphere (Defant and Drummond 1990). Also, the samples represent various Nb/Ta anomalies (0.14–0.84 with an average of 0.34), the same as Archean granitoids of the tonalite-trondhjemite-granodiorite suite and the early continental crust of Earth (e.g., Foley et al. 2002). They are generated from the partial melting of subducted oceanic slabs under eclogite or garnet–amphibolite conditions at the convergent margins (Defant and Drummond 1990). The La/Yb<sub>CN</sub> ratios of the samples (4.7–21.2) suggest that partial melting has occurred in garnet–amphibolite facies rather than in eclogite conditions (Foley et al. 2002). The REE<sub>CN</sub> patterns of the samples indicate that garnet was not a significant residual phase, and intracrustal partial melting happened at pressures below 10 kb (e.g., Taylor 1977). This process resulted in plagioclase fractionation and negative Eu anomaly in the source rocks.

The samples have a significant variation of Nb/Ta ratios (3.37–18.5) (Table 3), representing crustal recycling in the arc magmas (e.g., Foley et al. 2000). Niobium and Ta usually occur together in titanite and rutile, stable under high-pressure conditions in the source rocks. The low concentrations of Nb and Ta in the samples show that these minerals did not contribute significantly to the melting.

Shifting from the ACM to WPVZ in the Th/Yb versus Ta/Yb diagram may display tectonic evolution from low angle subduction to extensional volcanism regimes (e.g., Kremer

and Tishin 2017). This transition probably occurred due to the rollback of the Neotethys slab in the collision zone during subduction.

## Conclusions

Upper Cretaceous Sanandaj shale is immature, first-order sediment, and its terrigenous particles were eroded from intermediate to felsic source rocks in an active margin. In contrast to the generally Cretaceous humid climate, shale samples on the weathering index diagrams show the arid-semiarid climatic conditions of the source area. Therefore, the arid-semiarid climatic conditions/low chemical weathering of sediments is related to intense tectonic activity in the study area.

The correlations of Th–U ( $r=0.83$ ), Th–Zr ( $r=0.83$ ), and U–Zr ( $r=0.90$ ) indicate that zircon hosts both U and Th in the samples. The significant chemical resistance of zircon caused U-insensitive leaching behavior, and Th/U or U/Th ratios cannot reflect the paleoredox conditions and the intensity of chemical weathering. The weak linear correlation of Th/U–CIA and the opposite behavior of U/Th relative to other paleoredox indices support this suggestion.

The studied samples show ratios of Th/U (> 3.8) and Th/Sc (= ~0.4–0.7), a wide range of Eu/Eu\*<sub>SN</sub> (= 0.26–0.89), and an isochron age of  $125 \pm 39$  Ma with an initial  $^{87}\text{Sr}/^{86}\text{Sr}$  ratio of  $0.7106 \pm 0.0032$ . These characteristics show that sediments were mainly derived from the young differentiated continental Andean arcs of the Late Jurassic–Early Cretaceous.

The REE<sub>CN</sub> patterns of the samples are similar to those from the UCC, turbidites from the Phanerozoic continental arc and the young differentiated arc type in modern deep-sea. The stacking pattern of K8–K12 units and shale geochemistry indicates a transition from trench to fore-arc settings through time under reduced conditions. The upwelling of anoxic water due to Cretaceous volcanic activity led to a critical change in ocean chemistry.

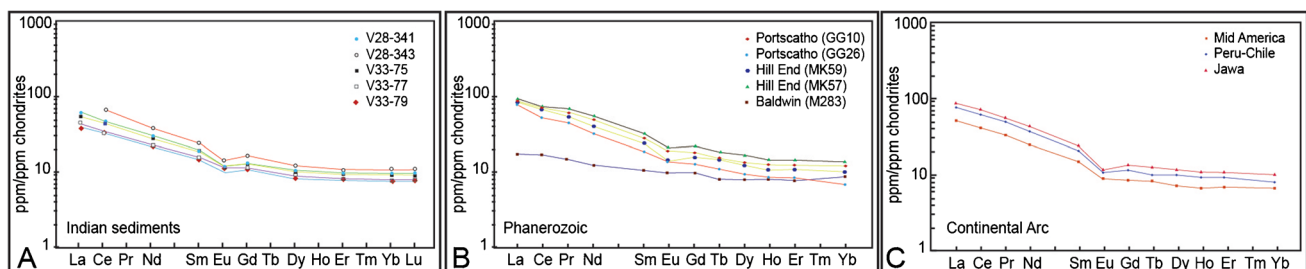


**Fig. 10** (A) REE<sub>CN</sub> patterns for Indian sediments (after Othman et al. 1989). (B) Selected REE<sub>CN</sub> patterns for graywacke-shale turbidites from Phanerozoic sequences deposited on active continental margins

(McLennan and Taylor 1991). (C) Typical REE<sub>CN</sub> patterns for modern deep-sea turbidites from continental arc tectonic settings (data from McLennan et al. 1990)

The shifting from the ACM to WPVZ fields in the Th/Yb versus Ta/Yb diagram may indicate the nature of tectonic evolution from low angle subduction to volcanism in an extensional tectonic setting.

**Acknowledgements** We would like to thank Professor Abdullah M. Al-Amri, the editor-in-chief of Arabian Journal of Geosciences, two anonymous reviewers, and Springer Nature Correction Team for their comments, and suggestions for improvements on final version of this work.

## Declarations

**Conflict of interest** The authors declare that they have no competing interests.

## References

- Agard P, Omrani J, Jolivet L, Mouthereau F (2005) Convergence history across Zagros (Iran): constraints from collisional and earlier deformation. *Int J Earth Sci (geologische Rundschau)* 94:401–419. <https://doi.org/10.1007/s00531-005-0481-4>
- Agard P, Omrani J, Jolivet L, Whitchurch H, Vrielynck B, Spakman W, Monié P, Meyer M, Wortel R (2011) Zagros orogeny: a subduction-dominated process. *Geol Mag* 148:692–725. <https://doi.org/10.1017/S001675681100046X>
- Alavi M (1994) Tectonics of the Zagros orogenic belt of Iran: new data and interpretations. *Tectonophys* 229(3–4):211–238. [https://doi.org/10.1016/0040-1951\(94\)90030-2](https://doi.org/10.1016/0040-1951(94)90030-2)
- Alavi M (2004) Regional stratigraphy of the Zagros fold-thrust belt of Iran and its proforland evolution. *J S Am Earth Sci* 304:1–20. <https://doi.org/10.2475/ajs.304.1.1>
- Alavi M (2007) Structures of the Zagros fold thrust belt in Iran. *J S Am Earth Sci* 307:1064–1095. <https://doi.org/10.2475/09.2007.02>
- Ao S, Xiao W, Jafari MK, Talebian M, Chen L, Wan B, Ji W, Zhang Z (2016) U-Pb zircon ages, field geology and geochemistry of the Kermanshah ophiolite (Iran): from continental rifting at 79 Ma to oceanic core complex at ca. 36 Ma in the southern Neo-Tethys. *Gondwana Res* 31:305–318. <https://doi.org/10.1016/j.gr.2015.01.014>
- Armstrong-Altrin JS, Lee YI, Kasper-Zubillaga JJ, Trejo-Ramírez E (2017) Mineralogy and geochemistry of sands along the Manzanillo and El Carrizal beach areas, southern Mexico: implications for palaeoweathering, provenance, and tectonic setting. *Geol J* 52(4):559–582. <https://doi.org/10.1002/gj.2792>
- Armstrong-Altrin JS, Ramos-Vázquez MA, Zavala-León AC, Montiel-García PC (2018) Provenance discrimination between Atasta and Alvarado beach sands, western Gulf of Mexico, Mexico: Constraints from detrital zircon chemistry and U-Pb geochronology. *Geol J* 53(6):2824–2848. <https://doi.org/10.1002/gj.3122>
- Armstrong-Altrin JS, Madhavaraju J, Vega-Bautista F, Ramos-Vázquez MA, Pérez-Alvarado BY, Kasper-Zubillaga JJ, Ekoa Bessa AZ (2021) Mineralogy and geochemistry of Tecolutla and Coatzacoalcos beach sediments. *SW Gulf of Mexico Appl Geochem* 134:105103. <https://doi.org/10.1016/j.apgeochem.2021.105103>
- Azizi H, Jahangiri A (2008) Cretaceous subduction-related volcanism in the northern Sanandaj-Sirjan Zone. *Iran J Geodyn* 45(4):178–190. <https://doi.org/10.1016/j.jog.2007.11.001>
- Azizi H, Moinevaziri H (2009) Review of the tectonic setting of Cretaceous to Quaternary volcanism in northwestern Iran. *J Geodyn* 47(4):167–179. <https://doi.org/10.1016/j.jog.2008.12.002>
- Azizi H, Asahara Y (2013) Juvenile granite in the Sanandaj-Sirjan zone, NW Iran: late Jurassic–early Cretaceous arc-continent collision. *Int Geol Rev* 55:1523–1540. <https://doi.org/10.1080/00206814.2013.782959>
- Azizi H, Hadad S, Stern RJ, Asahara Y (2019) Age, geochemistry, and emplacement of the ~40-Ma Baneh granite–appinite complex in a transpressional tectonic regime, Zagros suture zone, northwest Iran. *Int Geol Rev* 61:195–223. <https://doi.org/10.1080/00206814.2017.1422394>
- Azizi H, Stern RJ (2019) Jurassic igneous rocks of the central Sanandaj-Sirjan zone (Iran) mark a propagating continental rift, not a magmatic arc. *Terra Nova* 31(5):415–423. <https://doi.org/10.1111/ter.12404>
- Baier J, Audétat A, Keppler H (2008) The origin of the negative niobium tantalum anomaly in subduction zone magmas. *Earth Planet Sci Lett* 267:290–300. <https://doi.org/10.1016/j.epsl.2007.11.032>
- Bailey JC (1981) Geochemical criteria for a refined tectonic discrimination of orogenic andesites. *Chem Geol* 31:139–154. [https://doi.org/10.1016/0009-2541\(81\)90135-2](https://doi.org/10.1016/0009-2541(81)90135-2)
- Bailleul J, Robin C, Chanier F, Guillocheau F, Field BD, Ferrière J (2007) Turbidite systems in the inner forearc domain of the Hikurangi convergent margin (New Zealand): new constraints on the development of trench-slope basins. *J Sediment Res* 77(4):263–283. <https://doi.org/10.2110/jsr.2007.028>
- Bau M (1996) Controls on the fractionation of isovalent trace elements in magmatic and aqueous systems: evidence from Y/Ho, Zr/Hf and lanthanide tetrad effect. *Contrib Miner Petrol* 123:323–333. <https://doi.org/10.1007/s004100050159>
- Bau M, Dulski P (1996) Distribution of yttrium and rare-earth elements in the Penge and Kuruman iron-formations, Transvaal Supergroup, South Africa. *Precambrian Res* 79:37–55. [https://doi.org/10.1016/0301-9268\(95\)00087-9](https://doi.org/10.1016/0301-9268(95)00087-9)
- Bea F (1996) Residence of REE, Y, Th and U in granites and crustal protoliths; implications for the chemistry of crustal melts. *J Petrol* 37(3):521–552. <https://doi.org/10.1093/ptrology/37.3.521>
- Berberian M, King GCP (1981) Towards a paleogeography and tectonic evolution of Iran. *Can J Earth Sci* 18:210–265. <https://doi.org/10.12691/ajmm-2-3-1>
- Bhatia MR (1983) Plate tectonics and geochemical composition of sandstones. *J Geol* 91:611–627. <https://doi.org/10.1086/628815>
- Bhatia MR, Crook KAW (1986) Trace element characteristics of graywackes and tectonic setting discrimination of sedimentary basins. *Contrib Miner Petrol* 92:181–193. <https://doi.org/10.1007/BF00375292>
- Brooks CK (1970) The concentrations of zirconium and hafnium in some igneous and metamorphic rocks and minerals. *Geochim Cosmochim Acta* 34:411–416. [https://doi.org/10.1016/0016-7037\(70\)90117-1](https://doi.org/10.1016/0016-7037(70)90117-1)
- Brumsack H-J (2006) The trace metal content of recent organic carbon-rich sediments: implications for Cretaceous black shale formation. *Palaeogeogr Palaeoclimatol Palaeoecol* 232:344–361. <https://doi.org/10.1016/j.palaeo.2005.05.011>
- Cerny P, Meintzer RE, Anderson AJ (1985) Extreme fractionation in rare-element granitic pegmatites: selected examples of data and mechanisms. *Can Miner* 23:381–421
- Cherven VB (1986) Tethys-marginal sedimentary basins in western Iran. *Am Assoc Pet Geol Bull* 97:516–522. [https://doi.org/10.1130/0016-7606\(1986\)97%3c516:TSBIWI%3e2.0.CO;2](https://doi.org/10.1130/0016-7606(1986)97%3c516:TSBIWI%3e2.0.CO;2)
- Cisterna CE, Altenberger U, Mon R, Günter C, Gutierrez A (2018) The metamorphic basement of the southern Sierra de Aconquija, Eastern Sierras Pampeanas: provenance and tectonic setting of

- a Neoproterozoic back-arc basin. *J S Am Earth Sci* 82:292–310. <https://doi.org/10.1016/j.jsames.2017.09.028>
- Clift PD, Degan PJ, Hannigan R, Blusztajn J (2000) Sedimentary and geochemical evolution of the Dras forearc basin, Indus suture, Ladakh Himalaya, India. *Geol Soc Am Bull* 112:450–466. [https://doi.org/10.1130/0016-7606\(2000\)112%3c450:SAGEOT%3e2.0.CO;2](https://doi.org/10.1130/0016-7606(2000)112%3c450:SAGEOT%3e2.0.CO;2)
- Compston W, Pidgeon RT (1962) Rubidium-strontium dating of shales by the total-rock method. *J Geophys Res* 67:3493–3502. <https://doi.org/10.1029/JZ067i009p03493>
- Condie KC (1986) Geochemistry and tectonic setting of Early Proterozoic supracrustal rocks in the southwestern United States. *J Geol* 94:845–864. [https://doi.org/10.1016/S0166-2635\(08\)70162-2](https://doi.org/10.1016/S0166-2635(08)70162-2)
- Condie KC, Philip DNJ, Conway CM (1992) Geochemical and detrital mode evidence for two sources of Early Proterozoic. *Sediment Geol* 77:51–76. [https://doi.org/10.1016/0037-0738\(92\)90103-X](https://doi.org/10.1016/0037-0738(92)90103-X)
- Correia Neves JM, Lopes Nunes JE, Sahama TG (1974) High hafnium members of the zircon-hafnion series from the granite pegmatites of Zambézia, Mozambique. *Contrib Miner Petrol* 48:73–80. <https://doi.org/10.1007/BF00399111>
- Cox R, Lowe DR, Cullers RL (1995) The influence of sediment recycling and basement composition on evolution of mudrock chemistry in the southwestern United States. *Geochim Cosmochim Acta* 59:2919–2940. [https://doi.org/10.1016/0016-7037\(95\)00185-9](https://doi.org/10.1016/0016-7037(95)00185-9)
- Cullers RL (1994) The controls on the major and trace element variation of shales, siltstones, and sandstones of Pennsylvanian-Permian age from uplifted continental blocks in Colorado to platform sediment in Kansas, USA. *Geochim Cosmochim Acta* 58:4955–4972. [https://doi.org/10.1016/0016-7037\(94\)90224-0](https://doi.org/10.1016/0016-7037(94)90224-0)
- Cullers RL (2000) The geochemistry of shales, siltstones and sandstones of Pennsylvanian-Permian age, Colorado, USA: implications for provenance and metamorphic studies. *Lithos* 51:181–203. [https://doi.org/10.1016/S0024-4937\(99\)00063-8](https://doi.org/10.1016/S0024-4937(99)00063-8)
- Cullers RL (2002) Implications of elemental concentrations for provenance, redox conditions, and metamorphic studies of shales and limestones near Pueblo, CO, USA. *Chem Geol* 191:305–327. [https://doi.org/10.1016/S0009-2541\(02\)00133-X](https://doi.org/10.1016/S0009-2541(02)00133-X)
- Cullers RL, Podkovyrov VN (2000) Geochemistry of the Mesoproterozoic Lakhanda shales in southeastern Yakutia, Russia: implications for mineralogical and provenance control, and recycling. *Precambrian Res* 104:77–93. [https://doi.org/10.1016/S0301-9268\(00\)00090-5](https://doi.org/10.1016/S0301-9268(00)00090-5)
- Dabard MP (1990) Lower Brioverian Formations (Upper Proterozoic) of the Armorican Massif (France): geodynamic evolution of source areas revealed by sandstone petrography and geochemistry. *Sediment Geol* 69:45–58. [https://doi.org/10.1016/0037-0738\(90\)90100-8](https://doi.org/10.1016/0037-0738(90)90100-8)
- Dimalanta CB, Graciano P, Yumul GP, Imai A (2013) Geodynamic evolution of the Bagoio Mineral District: unlocking the Cenozoic record from clastic rocks. *J Asian Earth Sci* 65:118–130. <https://doi.org/10.1016/j.jseaes.2012.09.026>
- Dargahi S, Arvin M, Pan Y, Babaei A (2010) Petrogenesis of post-collisional A-type granitoids from the Urumieh-Dokhtar magmatic assemblage, Southwestern Kerman, Iran: constraints on the Arabian-Eurasian continental collision. *Lithos* 115(1–4):190–204. <https://doi.org/10.1016/j.lithos.2009.12.002>
- Defant MJ, Drummond MS (1990) Derivation of some modern arc magmas by melting of young subducted lithosphere. *Nature* 347:662–665. <https://doi.org/10.1038/347662a0>
- Dey S, Rai AK, Chaki A (2008) Widespread arkose along the northern margin of the Proterozoic Kaladgi basin, Karnataka: product of uplifted granitic source or K-metasomatism. *J Geol Soc India* 71:79–88
- Dinelli E, Lucchini F, Mordenti A, Paganelli L (1999) Geochemistry of Oligocene-Miocene sandstones of the northern Apennines (Italy) and evolution of chemical features in relation to provenance changes. *Sediment Geol* 127:193–207. [https://doi.org/10.1016/0009-2541\(88\)90136-2](https://doi.org/10.1016/0009-2541(88)90136-2)
- Dostal J, Keppie BL, Cousens JB, Murphy JB (1996) 550–580 Ma magmatism in Cape Breton Island (Nova Scotia, Canada): the product of NW-dipping subduction during the final stage of amalgamation of Gondwana. *Precambrian Res* 76:93–113. [https://doi.org/10.1016/0301-9268\(96\)00040-X](https://doi.org/10.1016/0301-9268(96)00040-X)
- Dostal J, Chatterjee AK (2000) Contrasting behavior of Nb/Ta and Zr/Hf ratios in a peraluminous granitic pluton (Nova Scotia, Canada). *Chem Geol* 163:207–218. [https://doi.org/10.1016/S0009-2541\(99\)00113-8](https://doi.org/10.1016/S0009-2541(99)00113-8)
- Draut AE, Clift P (2012) Basins in ARC-continent collisions. In: Busby C, Azor A. (eds) *Tectonics of Sedimentary Basins*. Camb Blackwell Sci 347–368. <https://doi.org/10.1002/9781444347166.ch17>
- Eby GN (1992) Chemical subdivision of the A-type granitoids: petrogenetic and tectonic implications. *Geol* 20:641–644. [https://doi.org/10.1130/0091-7613\(1992\)020%3c0641:CSOTAT%3e2.3.CO;2](https://doi.org/10.1130/0091-7613(1992)020%3c0641:CSOTAT%3e2.3.CO;2)
- Erturk MA, Beyarslan M, Chung SL, Lin TH (2018) Eocene magmatism (Maden Complex) in the Southeast Anatolian Orogenic Belt: magma genesis and tectonic implications. *Geosci Front* 9:1829–1847. <https://doi.org/10.1016/j.gsf.2017.09.008>
- Fedo CM, Nesbitt HW, Young GM (1995) Unraveling the effects of potassium metasomatism in sedimentary rocks and paleosols, with implications for weathering conditions and provenance. *Geol* 23:921–924. [https://doi.org/10.1130/0091-7613\(1995\)023%3c0921:UTEOPM%3e2.3.CO;2](https://doi.org/10.1130/0091-7613(1995)023%3c0921:UTEOPM%3e2.3.CO;2)
- Fedo CM, Eriksson KA, Krogstad EJ (1996) Geochemistry of shales from the Archean; 3.0 Ga Buhwa Greenstone Belt, Zimbabwe: implications for provenance and source-area weathering. *Geochim Cosmochim Acta* 60:1751–1763. [https://doi.org/10.1016/0016-7037\(96\)00058-0](https://doi.org/10.1016/0016-7037(96)00058-0)
- Fedo CM, Young GM, Nesbitt HW, Hanchar JM (1997) Potassic and sodic metasomatism in the Southern Province of the Canadian Shield: evidence from the Paleoproterozoic Serpent Formation, Huronian Supergroup, Canada. *Precambrian Res* 84:17–36. [https://doi.org/10.1016/S0301-9268\(96\)00058-7](https://doi.org/10.1016/S0301-9268(96)00058-7)
- Floyd PA, Leveridge BE (1987) Tectonic environment of the Devonian Gramscatho basin, south Cornwall: framework mode and geochemical evidence from turbiditic sandstones. *Geol Soc Lond Spec Publ* 144:531–542. <https://doi.org/10.1144/gsjgs.144.4.0531>
- Floyd PA, Kelling G, Gökçen SL, Gökçen N (1991) Geochemistry and tectonic environment of basaltic rocks from the Misis Ophiolitic Melange, south Turkey. *Chem Geol* 89:263–280. [https://doi.org/10.1016/0009-2541\(91\)90020-R](https://doi.org/10.1016/0009-2541(91)90020-R)
- Foley SF, Barth MG, Jenner GA (2000) Rutile/melt partition coefficients for trace elements and an assessment of the influence of rutile on the trace element characteristics of subduction zone magmas. *Geochim Cosmoch Acta* 64(5):933–938. [https://doi.org/10.1016/S0016-7037\(99\)00355-5](https://doi.org/10.1016/S0016-7037(99)00355-5)
- Foley S, Tiepolo M, Vannucci R (2002) Growth of early continental crust controlled by melting of amphibolite in subduction zones. *Nature* 417:837–840. <https://doi.org/10.1038/nature00799>
- Garver JI, Scott TJ (1995) Trace elements in shale as indicators of crustal provenance and terrane accretion in the southern Canadian Cordillera. *Geol Soc Am Spec Pap* 107:440–453. [https://doi.org/10.1130/0016-7606\(1995\)107%3c0440:TEISAI%3e2.3.CO;2](https://doi.org/10.1130/0016-7606(1995)107%3c0440:TEISAI%3e2.3.CO;2)
- Greber ND, Dauphas N (2019) The chemistry of fine-grained terrigenous sediments reveals a chemically evolved Paleoproterozoic

- emerged crust. *Geochim Cosmoch Acta* 255:247–264. <https://doi.org/10.1016/j.gca.2019.04.012>
- Ghasemi A, Talbot CJ (2006) A new tectonic scenario for the Sanandaj-Sirjan Zone (Iran). *J Asian Earth Sci* 26:683–693. <https://doi.org/10.1016/j.jseas.2005.01.003>
- Girty GH, Ridge DL, Knaak C, Johnson D, Al-Ryami R (1996) Provenance and depositional setting of Paleozoic chert and argillite, Sierra Nevada, California. *J Sediment Res* 66:107–118. <https://doi.org/10.1306/D42682CA-2B26-11D7-8648000102C1865D>
- Gorton MP, Schandl ES (2000) From continents to island arcs: a geochemical index of tectonic setting for arc-related and within-plate felsic to intermediate volcanic rocks. *Can Miner* 38:1065–1073. <https://doi.org/10.2113/gscanmin.38.5.1065>
- Green TH (1995) Significance of Nb/Ta as an indicator of geochemical processes in the crust mantle system. *Chem Geol* 120:347–359. [https://doi.org/10.1016/0009-2541\(94\)00145-X](https://doi.org/10.1016/0009-2541(94)00145-X)
- Guo Q, Xiao W, Windley BF, Mao Q, Han C, Qu J, Ao S, Li J, Song D, Yong Y (2012) Provenance and tectonic settings of Permian turbidities from the Beishan Mountains, NW China: implications for the Late Paleozoic accretionary tectonics of the southern Altaids. *J Asian Earth Sci* 49:54–68. <https://doi.org/10.1016/j.jseas.2011.03.013>
- Harnois L (1988) The CIW index: a new chemical index of weathering. *Sediment Geol* 55:319–322. [https://doi.org/10.1016/0037-0738\(88\)90137-6](https://doi.org/10.1016/0037-0738(88)90137-6)
- Hassanzadeh J, Wernicke BP (2016) The Neotethyan Sanandaj-Sirjan zone of Iran as an archetype for passive margin-arc transitions. *Tecton* 35:586–621. <https://doi.org/10.1002/2015TC003926>
- Hastie AR, Kerr AC, Pearce JA, Mitchell SF (2007) Classification of altered volcanic island arc rocks using immobile trace elements: development of the Th-Co discrimination diagram. *J Petrol* 48:2341–2357. <https://doi.org/10.1093/ptrology/egm062>
- Hatch JR, Leventhal JS (1992) Relationship between inferred redox potential of the depositional environment and geochemistry of the Upper Pennsylvanian (Missourian) Stark Shale Member of the Dennis Limestone, Wabausee County, Kansas, USA. *Chem Geol* 99(1–3):65–82. [https://doi.org/10.1016/0009-2541\(92\)90031-Y](https://doi.org/10.1016/0009-2541(92)90031-Y)
- Hay WW (1981) Sedimentological and geochemical trends resulting from the breakup of Pangaea. *Proc Int Geol Congr Geol Oceans Symp Paris Oceanolo Acta 4 (SP)* 135–147
- Hayashi K, Fujisawa H, Holland HD, Ohmoto H (1997) Geochemistry of 1.9 Ga sedimentary rocks from northeastern Labrador Canada. *Geochim Cosmochim Acta* 61:4115–4137. [https://doi.org/10.1016/S0016-7037\(97\)00214-7](https://doi.org/10.1016/S0016-7037(97)00214-7)
- Herron MM (1988) Geochemical classification of terrigenous sands and shales from core or log data. *J Sediment Res* 58:820–829. <https://doi.org/10.1306/D212F8E77-2B24-11D7-8648000102C1865D>
- Hessami K, Koyi HA, Talbot CJ (2001) The significance of strike-slip faulting in the basement of the Zagros fold and thrust belt. *J Petrol Geol* 24:5–28. <https://doi.org/10.1111/j.1747-5457.2001.tb00659.x>
- Holland HD (1984) *The chemical evolution of the atmosphere and oceans*. Princeton University Press, Princeton Ser N J, p 582
- Jenkyns HC (2010) Geochemistry of oceanic anoxic events. *Geochim Geophys Geosys* 11(3):1–30. <https://doi.org/10.1144/gsjgs.137.2.0171>
- Jian X, Guan P, Zhang W, Feng F (2013) Geochemistry of Mesozoic and Cenozoic sediments in the northern Qaidam basin, northeastern Tibetan Plateau: implications for provenance and weathering. *Chem Geol* 360–361:74–88. <https://doi.org/10.1016/j.chemgeo.2013.10.011>
- Jones B, Manning DC (1994) Comparison of geochemical indices used for the interpretation of paleo-redox conditions in ancient mudstones. *Chem Geol* 111(1–4):111–129. [https://doi.org/10.1016/0009-2541\(94\)90085-X](https://doi.org/10.1016/0009-2541(94)90085-X)
- Kasanzu C, Maboko MAH, Manya S (2008) Geochemistry of fine-grained clastic sedimentary rocks of the Neoproterozoic Ikorongo Group, NE Tanzania: implications for provenance and source rock weathering. *Precambrian Res* 164(3):201–221. <https://doi.org/10.1016/j.precamres.2008.04.007>
- Kelemen PB, Hanghoj K, Greene AR (2003) One view of the geochemistry of subduction-related magmatic arcs, with an emphasis on primitive andesite and lower crust. In: Holland, HD, Turekian, KK (eds) *Treatise on Geochemistry*. Elsevier-Pergamon, Oxford 593–659. <https://doi.org/10.1016/B0-08-043751-6/03035-8>
- Kilian R, Behrmann J (2003) Geochemical constraints on the sources of southern Chile trench sediments and their recycling in arc magmas of the Southern Andes. *Geol Soc Lond Spec Publ* 160:57–70. <https://doi.org/10.1144/0016-764901-143>
- Koch CF, Hansen TA (2021) Cretaceous period. *Encyclopedia Britannica*. <https://www.britannica.com/science/Cretaceous-Period>. Accessed 21 May 2021
- Kremer I, Tishin PA (2017) Composition and conditions of the late Mesozoic volcanism occurrence of the northern part of the Borschovochny ridge (Eastern Transbaikalia). *OP Conf Ser Earth and Environ Sci* 110. <https://doi.org/10.1088/1755-1315/110/1/012011>
- LeBas MJ, Le Maitre RW, Streckeisen A, Zanettin B (1986) A chemical classification of volcanic rocks based on the total alkali silica diagram. *J Petrol* 27:745–750. <https://doi.org/10.1093/ptrology/27.3.745>
- Lee YI (2002) Provenance derived from the geochemistry of late Paleozoic-early Mesozoic mudrocks of the Pyeongan Supergroup, Korea. *Sediment Geol* 149:219–235. [https://doi.org/10.1016/S0037-0738\(01\)00174-9](https://doi.org/10.1016/S0037-0738(01)00174-9)
- Martinez JI (2003) The paleoecology of Late Cretaceous upwelling events from the Upper Magdalena Basin, Colombia. *Palaios* 18:305–320. [https://doi.org/10.1669/0883-1351\(2003\)018%3c0305:TPOLCU%3e2.0.CO;2](https://doi.org/10.1669/0883-1351(2003)018%3c0305:TPOLCU%3e2.0.CO;2)
- McLennan SM (1989) Rare earth elements in sedimentary rocks: influence of provenance and sedimentary processes. *Rev Miner Geochem* 21:169–200. <https://doi.org/10.1515/9781501509032-010>
- McLennan SM (1993) Weathering and global denudation. *J Geol* 101:295–303. <https://doi.org/10.1086/648222>
- McLennan SM (2001) Relationship between the trace element composition of sedimentary rocks and upper continental crust. *Geochim Geophys Geosys* 2(4):1–24. <https://doi.org/10.1029/2000GC000109>
- McLennan SM, Nance WB, Taylor SR (1980) Rare earth element-thorium correlations in sedimentary rocks, and the composition of the continental crust. *Geochim Cosmochim Acta* 44:1833–1839. [https://doi.org/10.1016/0016-7037\(80\)90232-X](https://doi.org/10.1016/0016-7037(80)90232-X)
- McLennan SM, Taylor SR, Eriksson KA (1983) Geochemistry of Archean shales from the Pilbara Supergroup, Western Australia. *Geochim Cosmochim Acta* 47:1211–1222. [https://doi.org/10.1016/0016-7037\(83\)90063-7](https://doi.org/10.1016/0016-7037(83)90063-7)
- McLennan SM, Taylor SR, McCulloch TM, Maynard JB (1990) Geochemical and Nd-Sr isotopic composition of deep-sea turbidites: crustal evolution and plate tectonic associations. *Geochim Cosmochim Acta* 54:2015–2050. [https://doi.org/10.1016/0016-7037\(90\)90269-Q](https://doi.org/10.1016/0016-7037(90)90269-Q)
- McLennan SM, Taylor SR (1991) Sedimentary rocks and crustal evolution. Tectonic setting and secular trends. *J Geol* 99:1–21. <https://doi.org/10.1086/629470>
- McLennan SM, Hemming S, McDaniel DK, Hanson GN (1993) Geochemical approaches to sedimentation, provenance and tectonics. *Geol Soc Am Spec Pap* 285:21–40. <https://doi.org/10.1017/S001675681800050X>

- Mehdipour Ghazi J, Moazzen M (2015) Geodynamic evolution of the Sanandaj-Sirjan Zone, Zagros Orogen. *Iran Turk J Earth Sci* 24:513–528. <https://doi.org/10.3906/yer-1404-12>
- Mohajjel M, Fergusson CL (2000) Dextral transpression in Late Cretaceous continental collision, Sanandaj-Sirjan Zone, western Iran. *J Struct Geol* 22:1125–1139. [https://doi.org/10.1016/S0191-8141\(00\)00023-7](https://doi.org/10.1016/S0191-8141(00)00023-7)
- Morata D, Aguirre L, Féraud G, Belmar M (2005) Geodynamic implications of the regional very low-grade metamorphism in the Lower Cretaceous of the Coastal Range in Central Chile. 6th Int Symp Andean Geodyn Barcelona 531–534
- Nesbitt HW, Young YM (1982) Early Proterozoic climates and plate motions inferred from major element chemistry of lutites. *Nature* 299:715–717. <https://doi.org/10.1038/299715a0>
- Ohkouchi N, Kuroda J, Taira A (2015) The origin of Cretaceous black shales: a change in the surface ocean ecosystem and its triggers. *Proc Jpn Acad, Ser B* 91(7):273–291
- Othman DB, White WM, Patchett J (1989) The geochemistry of marine sediments, island arc magma genesis, and crust-mantle recycling. *Rev Earth Planet Sci Lett* 94:1–21. [https://doi.org/10.1016/0012-821X\(89\)90079-4](https://doi.org/10.1016/0012-821X(89)90079-4)
- Özdemir Y, Güleç N (2014) Geological and geochemical evolution of the Quaternary suphan stratovolcano, eastern Anatolia, Turkey: evidence for the lithosphere-asthenosphere interaction in post-collisional volcanism. *J Petrol* 55:37–62. <https://doi.org/10.1093/PETROLOGY/EGT060>
- Pearce JA (1983) Role of the subcontinental lithosphere in magma genesis at active continental margins. In: Hawkesworth CJ, Norry MJ (eds) *Continental Basalts and Mantle Xenoliths*. UK, Shiva Press, Nantwich, pp 230–249
- Peccerillo A, Taylor SR (1976) Geochemistry of Eocene calc-alkaline volcanic rocks from the Kastamonu area, northern Turkey. *Contrib Miner Petrol* 58(1):63–81. <https://doi.org/10.1007/BF00384745>
- Pettijohn FJ, Potter PE, Siever R (1987) *Sand and sandstone*. Springer-Verlag, Berl, p 553
- Plank T, Langmuir CH (1998) The chemical composition of subducting sediment and its consequences for the crust and mantle. *Chem Geol* 145:325–394. [https://doi.org/10.1016/S0009-2541\(97\)00150-2](https://doi.org/10.1016/S0009-2541(97)00150-2)
- Poldervaart A (1955) Chemistry of Earth's crust. In: Poldervaart A (ed) *Crust of the Earth*. Geol Soc Am Spec Pap 19–144
- Price JR, Velbel AM (2003) Chemical weathering indices applied to weathering profiles developed on heterogeneous felsic metamorphic parent rocks. *Chem Geol* 202:397–416. <https://doi.org/10.1016/j.chemgeo.2002.11.00>
- Rimmer SM (2004) Geochemical paleoredox indicators in Devonian-Mississippian black shales, Central Appalachian Basin (USA). *Chem Geol* 206:373–391. <https://doi.org/10.1016/j.chemgeo.2003.12.029>
- Rimmer SM, Thompson JA, Goodnight SA, Robl TL (2004) Multiple controls on the preservation of organic matter in Devonian-Mississippian marine black shales: geochemical and petrographic evidence. *Palaeogeogr Palaeoclimatol Palaeoecol* 215:125–154. <https://doi.org/10.1016/j.palaeo.2004.09.001>
- Rodríguez-Tovar FJ, Uchman A, Molina E, Monechi S (2010) Bioturbation redistribution of Danian calcareous nannofossils in the uppermost Maastrichtian across the K-Pg boundary at Bidart, SW France. *Geobios* 43:569–579. <https://doi.org/10.1016/j.geobios.2010.03.002>
- Rogers JJW, Adams JAS (1969) Uranium. In: Wedepohl KH (ed) *Handbook of Geochemistry*. Berl, Heidelb N. Y., Springer 11–14
- Roser BP, Korsch RJ (1986) Determination of tectonic setting of sandstone–mudstone suites using SiO<sub>2</sub> content and K<sub>2</sub>O/Na<sub>2</sub>O ratio. *J Geol* 94:635–650. <https://doi.org/10.1086/629071>
- Roser BP, Cooper RA, Nathan S, Tulloch AJ (1996) Reconnaissance sandstone geochemistry, provenance and tectonic settings of the Lower Paleozoic terrains of the West Coast and Nelson, New Zealand. *N Z J Geol and Geophys* 39:1–16. <https://doi.org/10.1080/00288306.1996.9514690>
- Roy DK, Roser BP (2013) Climatic control on the composition of Carboniferous-Permian Gondwana sediments, Khalaspir basin, Bangladesh. *Gondwana Res* 23:1163–1171. <https://doi.org/10.1016/j.jr.2012.07.006>
- Rudnick RL, Barth M, Horn I, McDonough WF (2000) Rutile-bearing refractory eclogites: missing link between continents and depleted mantle. *Sci* 287:278–281. <https://doi.org/10.1126/science.287.5451.278>
- Rudnick RL, Gao S (2003) Composition of the continental crust: the crust. *Treatise Geochem* 3:1–64. <https://doi.org/10.1126/science.287.5451.278>
- Schlanger SO, Arthur MA, Jenkyns HC, Scholle PA (1987) The Cenomanian-Turonian Oceanic Anoxic Event, I. Stratigraphy and distribution of organic carbon-rich beds and the marine  $\delta^{13}\text{C}$  excursion. In: Brooks, J, Fleet, AJ (eds) *Marine Petroleum Source Rocks*. Geol Soc Lond Spec Publ 26:371–399. <https://doi.org/10.1144/GSL.SP.1987.026.01.24>
- Şengör AMC (1990) A new model for the late Paleozoic-Mesozoic tectonic evolution of Iran and implications for Oman. *Geol Soc Lond Spec Publ* 49:797–831. <https://doi.org/10.1144/GSL.SP.1992.049.01.49>
- Shahabpour J (2005) Tectonic evolution of the orogenic belt in the region located between Kerman and Neyriz. *J Asian Earth Sci* 24(4):405–417. <https://doi.org/10.1016/j.jseaes.2003.11.007>
- Shahbazi H, Siebel W, Pourmoafee M, Ghorbani M, Sepahi AA, Shang CK, Vousoughi Abedini M (2010) Geochemistry and U-Pb zircon geochronology of the Alvand plutonic complex in Sanandaj-Sirjan zone (Iran): new evidence for Jurassic magmatism. *J Asian Earth Sci* 39:668–683. <https://doi.org/10.1016/j.jseaes.2010.04.014>
- Shaw DM (1968) A review of K-Rb fractionation trends by covariance analysis. *Geochim Cosmochim Acta* 32:573–601. [https://doi.org/10.1016/0016-7037\(68\)90050-1](https://doi.org/10.1016/0016-7037(68)90050-1)
- Stöcklin J (1968) Structural history and tectonics of Iran, a review. *Am Assoc Pet Geol Bull* 52:1229–1258. <https://doi.org/10.1306/5D25C4A5-16C1-11D7-8645000102C1865D>
- Stöcklin J, Nabavi M (1972) Tectonic map of Iran, Scale 1:2500000. Geol Surv Iran
- Sugisaki R (1980) Major element chemistry of the Japan trench sediments, Legs 56 and 57, Deep Sea Drilling Project. Initial Rep DSDP 56(57):1233–1248
- Suttner LJ, Dutta PK (1986) Alluvial sandstone composition and paleoclimate; I, Framework mineralogy. *J Sediment Petrol* 56:329–345. <https://doi.org/10.1306/212F8909-2B24-11D7-8648000102C1865D>
- Talebian M, Jackson J (2004) A reappraisal of earthquake focal mechanisms and active shortening in the Zagros mountains of Iran. *Geophys J Int* 156:506–526. <https://doi.org/10.1111/j.1365-246X.2004.02092.x>
- Taylor SR (1977) Island arc models and the composition of the continental crust. In: Talwani M, Pitman WC (eds) *Island arcs, deep-sea trenches, and back arc basins*. Am Geophys Union Maurice Ewing Ser 325–335. <https://doi.org/10.1029/ME001p0325>
- Taylor SR, McLennan SM (1985) *The Continental Crust: its composition and evolution. An examination of the geochemical record preserved in sedimentary rocks*. Blackwell Sci, Oxford 312

- Taylor SR, McLennan SM (1995) The geochemical evolution of the continental crust. *Rev Geophys* 33:241–265. <https://doi.org/10.1029/95RG00262>
- Trabucho-Alexandre J, Van Gilst RI, Rodriguez-López JP, de Boer PL (2011) The sedimentary expression of oceanic anoxic event 1b in the North Atlantic. *Sediment* 58:1217–1246. <https://doi.org/10.1111/j.1365-3091.2010.01202.x>
- Trabucho-Alexandre J, Hay WW, de Boer PL (2012) Phanerozoic environments of black shale deposition and the Wilson Cycle. *Solid Earth* 3:29–42. <https://doi.org/10.5194/se-3-29-2012>
- Uchman A, Abbassi N, Naeji MR (2005) Persichnusigen. nov, associated ichnofossils from the upper Cretaceous to Eocene deep-sea deposits of the Sanandaj area. *West Iran Ichnos* 12:141–149. <https://doi.org/10.1080/10420940590914624>
- Wang BQ, Wang W, Zhou M-F (2013) Provenance and tectonic setting of the Triassic Yidun Group, the Yidun Terrane. *Tibet Geosci Front* 4(6):765–777. <https://doi.org/10.1016/j.gsf.2013.02.007>
- Wang L, Huang CC, Pang J, Zha X, Zhou Y (2014) Paleofloods recorded by slack-water deposits in the upper reaches of the Hanjiang River valley, middle Yangtze River basin, China. *J Hydrol* 519:1249–1256. <https://doi.org/10.1016/j.jhydrol.2014.08.002>
- Wang W, Zhou M-F (2012) Sedimentary records of the Yangtze Block (South China) and their correlation with equivalent Neoproterozoic sequences on adjacent continents. *Sediment Geol* 265–266:126–142. <https://doi.org/10.1016/j.precamres.2011.10.010>
- Wang W, Zhou M-F, Yan D-P, Li JW (2012) Depositional age, provenance, and tectonic setting of the Neoproterozoic Sibao Group, southeastern Yangtze Block, South China. *Precambrian Res* 192–195:107–124. <https://doi.org/10.1016/j.precamres.2011.10.010>
- Wang W, Zhou M-F (2013) Petrological and geochemical constraints on provenance, paleoweathering, and tectonic setting of the neoproterozoic sedimentary basin in the Eastern Jiangnan Orogen. *South China J Sediment Res* 83(11):974–993. <https://doi.org/10.2110/jsr.2013.74>
- Wang Z, Yan Z, Ma Z, He S, Fu C, Wang D (2016) Geochronological and geochemical evidence of amphibolite from the Hualong Group, northwest China: implication for the early Paleozoic accretionary tectonics of the Central Qilian belt. *Lithos* 248–251:12–21. <https://doi.org/10.1016/j.lithos.2016.01.012>
- Wedepohl KH (1978) Manganese: abundance in common sediments and sedimentary rocks. *Handb Geochem*, Springer Berl 1–17
- Whitman J, Baltuck M, Haggerty J, Dean W (1985) Turbidite sedimentology and history of the East Mariana basin. In: Moberly R, Schlanger SO, Baltuck M, Bergen JA, Dean W, Floyd PA, Fujii N, Haggerty JA, Ogg JG, Premoli Silva I, Schaaf A, Schaefer RG, Sliter WV, Whitman JM (eds) *Initial Rep Deep Sea*. US Gov Print Off Wash 365–387
- Willis KM, Stern RJ, Clauer N (1988) Age and geochemistry of late Precambrian sediments of the Hammamat series from the Northeastern Desert of Egypt. *Precambrian Res* 42:173–187. [https://doi.org/10.1016/0301-9268\(88\)90016-2](https://doi.org/10.1016/0301-9268(88)90016-2)
- Winchester JA, Floyd PA (1977) Geochemical discrimination of different magma series and their differentiation products using immobile elements. *Chem Geol* 20:325–343. [https://doi.org/10.1016/0009-2541\(77\)90057-2](https://doi.org/10.1016/0009-2541(77)90057-2)
- Wronkiewicz DJ, Condie KC (1987) Geochemistry of Archean shales from the Witwatersrand Supergroup, South Africa: source-area weathering and provenance. *Geochim Cosmoch Acta* 51:2401–2416. [https://doi.org/10.1016/0016-7037\(87\)90293-6](https://doi.org/10.1016/0016-7037(87)90293-6)
- Yamamoto K, Sugisaki R, Arai F (1986) Chemical aspects of alteration of acidic tufts and their application to siliceous deposits. *Chem Geol* 55:61–76. [https://doi.org/10.1016/0009-2541\(86\)90128-2](https://doi.org/10.1016/0009-2541(86)90128-2)
- Zahedi M, Hajian J (1985) Geology map of Sanandaj. Scale 1:250000. No. C5. *Geol Surv Iran*
- Zhai L, Wu C, Ye Y, Zhang S, Wang Y (2018) Fluctuations in chemical weathering on the Yangtze Block during the Ediacaran-Cambrian transition: implications for paleoclimatic conditions and the marine carbon cycle. *Palaeogeogr Palaeoclimatol Palaeoecol* 490:280–292. <https://doi.org/10.1016/j.palaeo.2017.11.006>

Springer Nature or its licensor holds exclusive rights to this article under a publishing agreement with the author(s) or other rightsholder(s); author self-archiving of the accepted manuscript version of this article is solely governed by the terms of such publishing agreement and applicable law.